Journal of Magnetic Resonance 304 (2019) 62–77

Contents lists available at ScienceDirect

Journal of Magnetic Resonance

journal homepage: www.elsevier.com/locate/jmr

Frequency selective coherence transfer NMR spectroscopy to study the structural dynamics of high molecular weight proteins

Yuki Toyama, Ichio Shimada *

Graduate School of Pharmaceutical Sciences, The University of Tokyo, Hongo, Bunkyo-ku, Tokyo 113-0033, Japan

ARTICLE INFO

Article history:
Received 19 March 2019
Revised 5 May 2019
Accepted 14 May 2019
Available online 15 May 2019

Keywords:
Heteronuclear coherence transfer
Solution NMR spectroscopy
High molecular weight protein
Protein dynamics
CPMG relaxation dispersion, CEST

ABSTRACT

Multidimensional nuclear magnetic resonance (NMR) spectroscopy has enabled detailed characterizations of protein structures and dynamics that are closely linked to functions. However, it leads to a large sensitivity loss in applications to high molecular weight proteins, which is caused by spin relaxation during the frequency discrimination period in the indirect dimension. Here, we describe a selective coherence transfer scheme, which enables us to selectively observe ^{1}H nuclei bonded to ^{15}N or ^{13}C nuclei with specified resonance frequencies. By utilizing this scheme, we achieved a 2.5- to 6-fold increase in signal height per unit of time with this scheme by avoiding the relaxation loss in the indirect dimension, as compared to the conventional two-dimensional heteronuclear correlation spectroscopy. We also demonstrated the effectiveness of this approach with applications to the membrane protein KirBac1.1, and characterized the functionally relevant conformational exchange process in both detergent micelles and a reconstituted membrane environment, corresponding to the apparent molecular masses of 220 kDa and 300 kDa, respectively.

1. Introduction

Solution nuclear magnetic resonance (NMR) spectroscopy has emerged as a powerful technique for studying protein structures, interactions, and dynamics on timescales ranging from picosecond to second, under physiological conditions. In biomolecular applications of NMR, we usually conduct multidimensional NMR experiments with ^{15}N- and/or ^{13}C- enriched samples, by exciting the ^{1}H nuclei and then transferring the initial ^{1}H magnetization to the scalar-coupled ^{15}N and/or ^{13}C nuclei [1–5]. With these techniques, we extend the crowded ^{1}H NMR spectra in an additional dimension labeled with a ^{15}N or ^{13}C resonance frequency, and thus we can avoid severe signal overlaps and comprehensively analyze the ^{1}H-^{15}N and/or ^{1}H-^{13}C correlations of proteins. In conventional multidimensional NMR experiments, the initial ^{1}H magnetizations are transferred to the attached ^{15}N or ^{13}C nuclei during the preparation and mixing periods, and then the frequency discrimination in the indirect ^{15}N or ^{13}C dimension is performed by recording multiple interferograms obtained with increased delays, which are subsequently subjected to a Fourier transformation.

The multidimensional NMR spectroscopy has enabled detailed characterizations of protein structures and dynamics that are closely relevant to physiological functions, however, it leads to a substantial loss in sensitivity when applied to high molecular weight proteins [6], membrane proteins [7], and proteins inside living-cells (*in-cell* NMR) [8]. In these applications, the effective rotational correlation times of proteins greatly increase and hence a large part of the observable magnetization is lost, due to spin relaxation during the magnetization transfer and frequency discrimination periods. For example, in order to resolve the resonances of proteins that differ in a few tens of Hz in the indirect dimension, we have to evolve the magnetization for tens to hundreds of milliseconds during the frequency discrimination period. Assuming a molecular mass of over 20 kDa, which roughly corresponds to a rotational correlation time longer than 10 ns as estimated on the basis of Stokes' law [9], the relaxation loss is expected to be at least several tens of percent. This limited sensitivity also greatly hampers the quantitative evaluations of protein dynamics proved by specifically designed relaxation experiments, such as Carr-Purcell-Meiboom-Gill (CPMG) relaxation dispersion (RD) [10–12] and chemical exchange saturation transfer (CEST) [13] experiments, which require the quantifications of signal intensities with a few percent of accuracy. Therefore, it has become increasingly important to develop NMR methodologies that can be extended to these biologically important, but challenging systems.

* Corresponding author.
E-mail address: shimada@iw-nmr.f.u-tokyo.ac.jp (I. Shimada).

https://doi.org/10.1016/j.jmr.2019.05.004
1090-7807/

Although multidimensional NMR experiments are mandatory to comprehensively analyze the NMR spectra of proteins, it is not always necessary to cover the entire bandwidth in the indirect dimension in practical applications. This is because we can usually identify the signals that serve as sensitive probes for the functional states of proteins (hereafter referred to as "probe signals") [14–17]. Therefore, if we can selectively observe these probe signals by utilizing *a priori* knowledge of their resonance frequencies, then we can improve the signal sensitivity per unit of time by avoiding the relaxation loss during the frequency discrimination period, and characterize the functional states of proteins more deeply and accurately from them. It would also be helpful to improve the signal sensitivity in the relaxation experiments, because the sensitivity loss during the relaxation delay and the requirements to measure the multiple two-dimensional (2D) spectra usually preclude us from obtaining high quality data that enable the extractions of accurate exchange parameters. To date, several sophisticated methods for selectively observing the probe signals have been developed [18–24]. However, because these methods rely on the use of relatively long selective pulses or spin-lock field irradiations, a substantial relaxation loss usually occurs during these irradiation periods, and hence their applications to high molecular weight proteins have been very limited. In addition, these methods were mainly applied to simple scalar-coupled two-spin systems, and thus their applicability to side-chain methyl spin systems in high molecular weight proteins has not been demonstrated [25,26].

In this report, we describe an optimized coherence transfer scheme utilizing a single-field polarization transfer, which enables us to selectively observe ^{1}H nuclei bonded to ^{15}N or ^{13}C nuclei with specified resonance frequencies. Although the intrinsic sensitivity and the coherence transfer efficiency were almost the same with the conventional two-dimensional spectroscopy, we could achieve a 2- to 6-fold increase in the sensitivity per unit of time with this scheme by avoiding the relaxation loss in the indirect dimension. We demonstrated that this scheme can be efficiently applied to both the amide ^{1}H-^{15}N and side-chain methyl $^{1}H_3$-^{13}C spin systems in high molecular weight proteins. We also incorporated the selective coherence transfer scheme in CPMG RD and CEST experiments, and showed that we could quantitatively characterize the conformational dynamics of proteins by selectively observing the probe signals. The effectiveness of this approach was also demonstrated with applications to the membrane protein KirBac1.1, in both detergent micelles and a reconstituted membrane environment, corresponding to apparent molecular masses of about 220 kDa and 300 kDa, respectively.

2. Results

2.1. Coherence transfer by selective continuous-wave irradiations.

Considering that the signal sensitivity is dependent on the magnitudes of the gyromagnetic ratios of the excited and observed nuclei, it is desirable to design experiments which directly excite and detect ^{1}H nuclei with the highest gyromagnetic ratio among the spin 1/2 nuclei in proteins. Therefore, we focused on scalar-coupled ^{1}H-A (A = ^{13}C or ^{15}N) two-spin systems, and aimed to observe the ^{1}H nuclei bonded to the A nuclei with specified resonance frequencies, by utilizing coherence transfer via scalar-coupling. In order to selectively irradiate the A nuclei, we used a selective continuous-wave (CW) irradiation, with strength on the intermediate perturbation regime, i.e., between the effective transverse relaxation rate and the *J*-coupling constant [2], because we can selectively perturb the spin polarization with a short irradiation time, as compared to phase- and amplitude- modulated selective pulses.

Fig. 1a shows the proposed coherence transfer scheme in the ^{1}H-^{15}N two-spin system, in which the selective CW irradiation is applied to the scalar-coupled ^{15}N during a ^{1}H spin-echo sequence. The scheme is analogous to the modified cross polarization scheme proposed by Pelupessy and Chiarparin [20], and the single field polarization transfer (SFPT) scheme proposed by Castellanos *et al.* [27], in which selective CW irradiation is applied to the ^{1}H nuclei, and not to the heteronuclei. We hereafter refer to this scheme as heteronuclear SFPT (HSFPT). In order to test this scheme, we first applied the HSFPT scheme to the ^{1}H-^{15}N two-spin system of [indole-^{15}N] DL-Tryptophan ($J = -98.7$ [Hz]), and compared the results with those obtained using the conventional insensitive nuclei enhanced by polarization transfer (INEPT) scheme [28] (Fig. 1b). We separately recorded in-phase H_y and anti-phase $2H_xN_z$ coherences, expressed by using the Cartesian product operators [9], by changing the phases of the ^{15}N pulses immediately before the detection period, and then quantitatively evaluated the efficiency of coherence transfer. When we used the CW field of 55 Hz, which is about half of the *J*-coupling constant, the in-phase H_y coherence diminished and successively evolved into the anti-phase $2H_xN_z$ coherence as the transfer time τ became longer (Figs. 1a and S1). This result indicates that we can achieve coherence transfer between the ^{1}H and ^{15}N nuclei by applying the CW field to the ^{15}N nuclei, which is similar to that observed in the conventional INEPT scheme (Fig. 1b). The key difference between these two schemes is the rate of the coherence transfer, as shown in the plots of the amounts of the coherences as a function of τ (Fig. 1c). In the INEPT scheme, the in-phase H_y and anti-phase $2H_xN_z$ coherences oscillate with the frequency of πJ, and hence the complete transfer to the anti-phase was achieved at around 5 ms ($\sim 1/2|J|$) and the inversion of the in-phase coherence was achieved at around 10 ms ($\sim 1/|J|$). In the HSFPT scheme, the efficient transfer to the anti-phase coherence and the inversion of the in-phase coherence were achieved at around 9 and 13 ms, respectively, and both were slightly longer than those in the INEPT scheme. We also observed similar results in the ^{1}H-^{13}C two-spin system of [ring-2-^{13}C] L-Histidine ($J = 221.7$ [Hz]) (Fig. S2).

In order to gain physical insights into the coherence transfer efficiency, we described the transfer of magnetization in a tilted doubly rotating frame [20]. Here, we assume a weakly-coupled ^{1}H-A two-spin system with a scalar coupling constant *J*, and a CW irradiation with the amplitude of ω_{rf} is applied to the A nuclei after an initial $\pi/2$ H_y pulse to create an in-phase H_x coherence. We also assume that the system is on-resonance for both the ^{1}H and A nuclei. Then, the Hamiltonian in the doubly rotating frame can be expressed by the following equation.

$$\mathcal{H} = \omega_{rf} A_x + 2\pi J H_z A_z \tag{1}$$

We can define the tilted doubly rotating frame by performing a rotation of $-\pi/2$ about the *y* axis for both spins. The Hamiltonian in the frame is expressed by the following equation.

$$\mathcal{H}^T = \omega_{rf} A_z + 2\pi J H_x A_x \tag{2}$$

This Hamiltonian can be rewritten in terms of single transition operators spanning the double quantum (DQ) and zero quantum (ZQ) spaces.

$$\begin{aligned} &\mathcal{H}^T = -\omega_{rf} ZQ_z + \pi J ZQ_x + \omega_{rf} DQ_z + \pi J DQ_x \\ &ZQ_z = \frac{H_z - A_z}{2}, \qquad DQ_z = \frac{H_z + A_z}{2} \\ &ZQ_x = H_x A_x + H_y A_y, \qquad DQ_x = H_x A_x - H_y A_y \\ &ZQ_y = H_y A_x - H_x A_y, \qquad DQ_y = H_y A_x + H_x A_y \end{aligned} \tag{3}$$

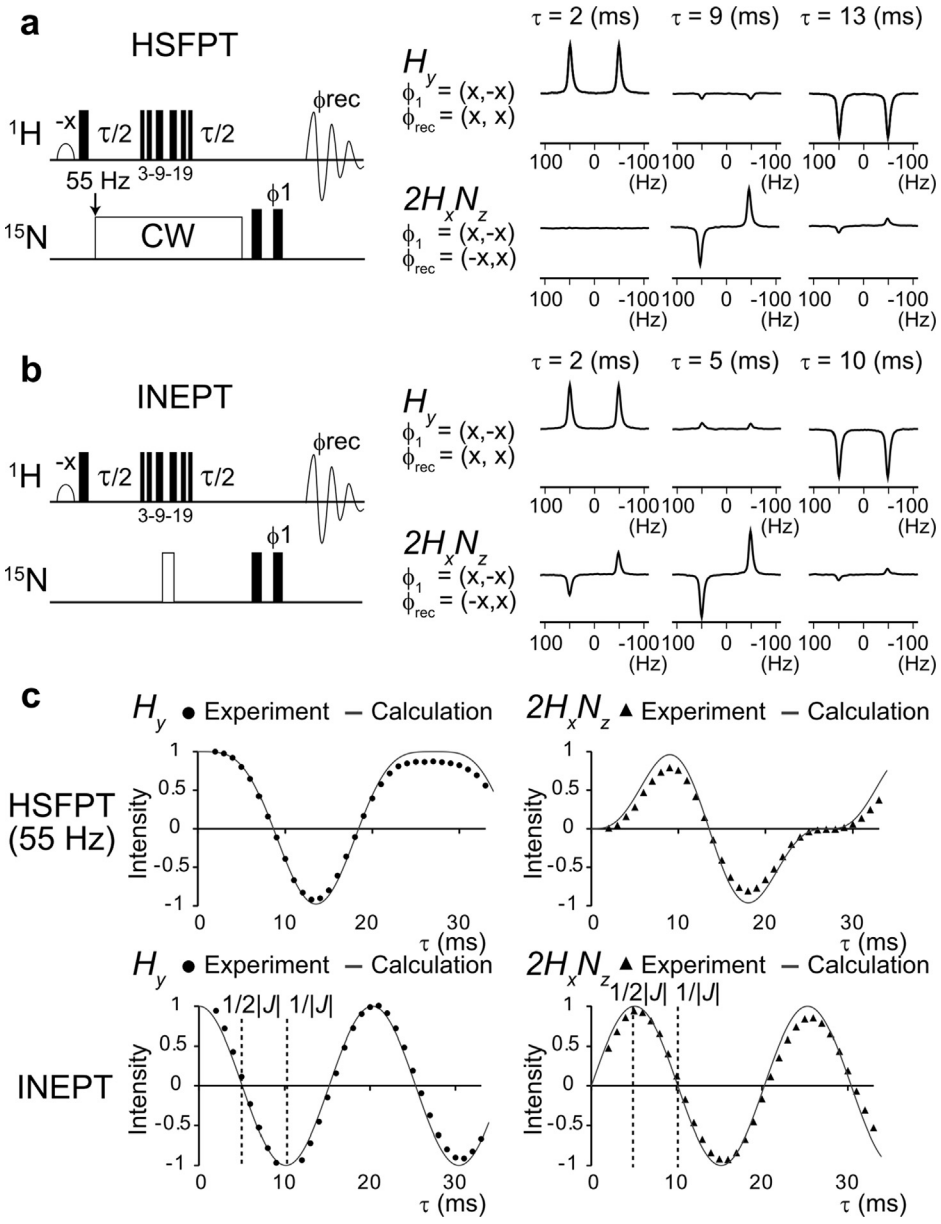

Fig. 1. Coherence transfer experiments in the ^{1}H-^{15}N two-spin system using the HSFPT and INEPT schemes. (a) The pulse sequence of the ^{15}N-selective HSFPT ^{1}H 1D with selective detections of the in-phase H_y and anti-phase $2H_xN_z$ coherences (left). ^{15}N-selective HSFPT ^{1}H 1D spectra of [indole-^{15}N] DL-Tryptophan with different transfer times τ are shown (right). The CW field strength was set to 55 Hz. Unless otherwise specified, pulse phases are along the $\times$ axis. Filled and open rectangles represent 90° and 180° pulses, respectively. (b) The pulse sequence of the ^{15}N-edited INEPT ^{1}H 1D with selective detections of the in-phase H_y and anti-phase $2H_xN_z$ coherences (left). ^{15}N-edited INEPT ^{1}H 1D spectra of [indole-^{15}N] DL-Tryptophan with different transfer times τ are shown (right). (c) Plots of the signal intensities observing the in-phase H_y or anti-phase $2H_xN_z$ coherences as a function of τ. Dots (H_y) and triangles ($2H_xN_z$) represent the experimentally observed values, and the lines represent the simulated values obtained from the density matrix calculations.

The vector representations of the coherence transfer in the DQ and ZQ spaces are shown in Fig. S3. If the initial density operator can be represented as $ZQ_z + DQ_z$ (H_x in the original frame), then the coherence transfer can be represented as the precession of the ZQ_z and DQ_z components around the effective field, $\omega_{eff} = \sqrt{\omega_{rf}^2 + \pi^2 J^2}$. Under the conditions that the ω_{rf} value is equal to $\pi|J|$ ($|J|/2$ in Hz) and the π refocus pulse about the z axis (π refocus pulse about the $\times$ axis in the original frame) is applied at the center of the period, the initial density operator, $ZQ_z + DQ_z$, evolves into the transverse component $-ZQ_y - DQ_y$ ($=2H_yA_z$ in the original frame) and subsequently to $-ZQ_z - DQ_z$ ($=-H_x$ in the original frame) around the effective field, $\omega_{eff} = \sqrt{2}\pi|J|$, which describes the experimentally observed coherence transfer in the previous section. Our numerical calculations showed that we can achieve the most efficient transfer to $-ZQ_y - DQ_y$ and the complete inversion to $-ZQ_z - DQ_z$, with the total transfer times of $0.94/|J|$ and $\sqrt{2}/|J|$, respectively.

Collectively, these results demonstrate that the selective coherence transfer via scalar-coupling can be achieved by applying the CW field to heteronuclei, if the CW field of $|J|/2$ Hz is sufficiently weak to discriminate the different spins of the microenvironments. For the backbone amide ^{1}H-^{15}N ($J \sim -90$ Hz) and the aliphatic ^{1}H-^{13}C ($J \sim 120$–150 Hz) two-spin systems, the CW field of $|J|/2$ Hz is usually sufficiently weak for discriminating the different spins in proteins, thus making it feasible to apply this scheme for selectively observing ^{1}H signals with improved sensitivity.

2.2. ^{15}N-selective HSFPT ^{1}H 1D experiments and comparisons with ^{1}H-^{15}N HSQC

We then applied the HSFPT scheme to observe the backbone amide ^{1}H-^{15}N correlations in high molecular weight proteins, and compared the results with those obtained from a heteronuclear single quantum coherence (HSQC) experiment (Fig. 2a), which is based on the conventional INEPT scheme. Fig. 2b shows the pulse sequence for measuring the ^{15}N-selective HSFPT ^{1}H 1D spectrum, in which the CW field is applied to the ^{15}N nuclei to selectively observe amide ^{1}H-^{15}N correlations of interest. In the ^{15}N-selective HSFPT ^{1}H 1D experiments, the in-phase H_y coherence coupled to the irradiated ^{15}N is selectively phase-inverted, and then the differential spectrum with and without the CW irradiation is obtained to subtract the rest of the ^{1}H signals. As mentioned in the previous section, we can achieve a phase-inversion of the in-phase H_y coherence most efficiently, when we use the CW filed of $|J|/2$ Hz and the total transfer time of $\sqrt{2}/|J|$. However, as the relaxation loss during the transfer period is severe in high molecular weight proteins, the shorter transfer time to avoid the relaxation loss is optimal for achieving maximum sensitivity. At the same time, the use of a slightly stronger CW field is beneficial under the conditions of a short transfer time, because the in-phase H_y coherence evolves faster with the stronger CW field (Figs. S1 and S2). In order to quantitatively evaluate these contributions and find the optimal conditions for high molecular weight proteins, we calculated a homogenous master equation for the ^{1}H-^{15}N two-spin system, following the formalism introduced by Allard *et al.* [29], which includes both the radio frequency and relaxation superoperators. We found that we can efficiently invert the in-phase H_y coherence by using a CW field of about 50 Hz and the total transfer time of about 12 ms for proteins with the rotational correlation time of 10–30 ns, therefore, we hereafter adopted these conditions (Fig. S4). Under these conditions, we observed ^{1}H-^{15}N HSQC and ^{15}N-selective HSFPT ^{1}H 1D spectra of [Val-^{15}N] maltose binding protein bound to β-cyclodextrin (MBP)

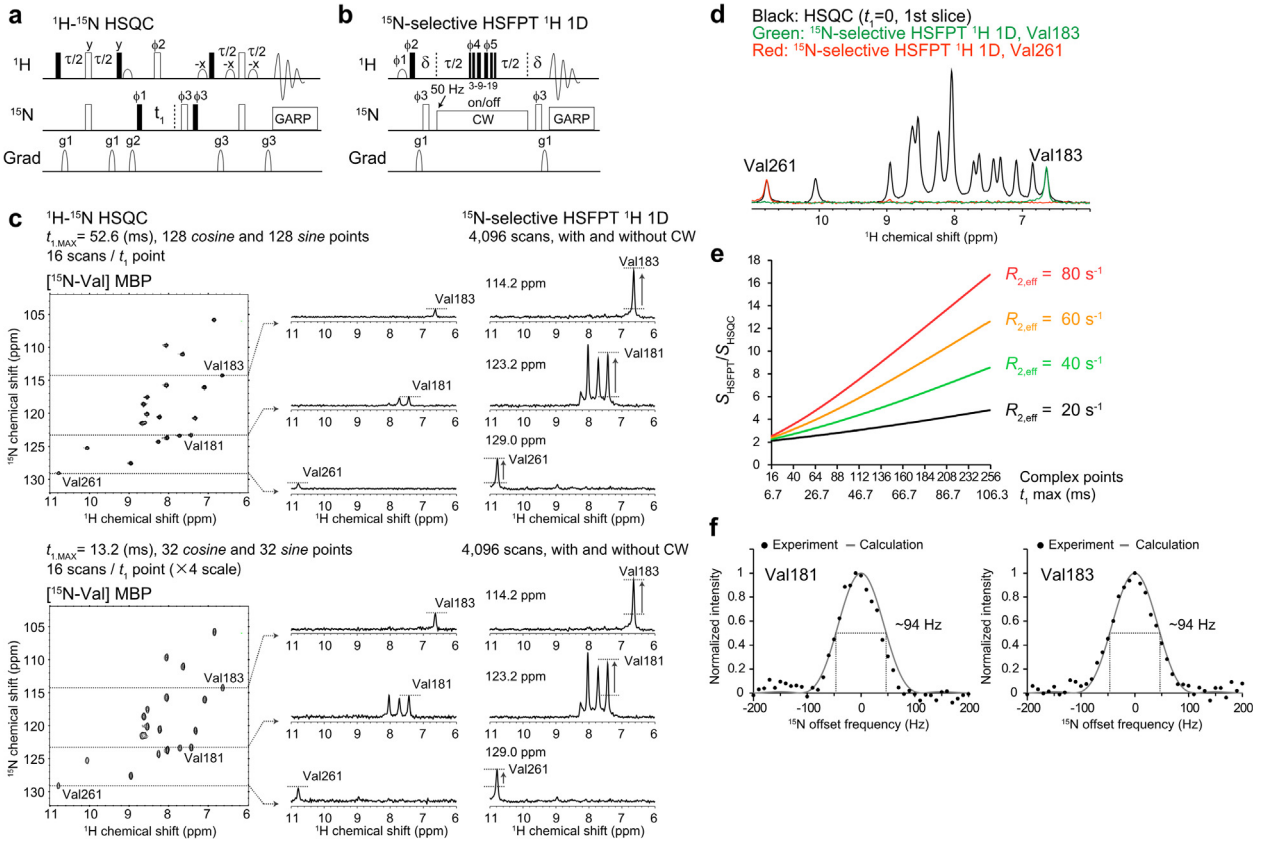

Fig. 2. ^{1}H-^{15}N HSQC and ^{15}N-selective HSFPT ^{1}H 1D spectra of [^{15}N-Val] MBP. (a) The pulse sequence of the ^{1}H-^{15}N HSQC. Unless otherwise specified, pulse phases are along the × axis. Filled and open rectangles represent 90° and 180° pulses, respectively. Open shapes represent water selective 90° pulses. The value of the INEPT transfer time τ is set to 5.5 ms. The ^{15}N decoupling during acquisition is achieved with a 1.3 kHz GARP4 field [90]. The following phase cycling scheme is used: ϕ1 = {x, $-x$}; ϕ2 = {2(x), 2($-x$)}; ϕ3 = {4(x), 4($-x$)}; receiver = {x, $-x$, x, $-x$, $-x$, x, $-x$, x}. Quadrature detection is achieved via states-TPPI of phase ϕ1 [91]. The duration and the amplitude of the sine-shaped pulsed magnetic field gradient applied along the z axis: G1 = (1 ms, 25 G/cm); G2 = (1 ms, 40 G/cm); G3 = (1 ms, 15 G/cm). (b) The pulse sequence of the ^{15}N-selective HSFPT ^{1}H 1D. The CW field strength is set to 50 Hz, and the value of the transfer time τ is set to 12 ms. δ denotes a short-delay for compensating the gradient pulse length. The following phase cycling scheme is used: ϕ1 = {$-x$, x}; ϕ2 = {x, $-x$}; ϕ3 = {4(y), 4($-y$)}; ϕ4 = {2(x), 2($-x$)}; ϕ5 = {2($-x$), 2(x)}; receiver = {x, $-x$}. The spectra with or without the CW irradiation are acquired alternately, and a difference spectrum between them is recorded. The 3–9–19 sequence can be replaced with a water flip-back sequence. The duration and the amplitude of the sine-shaped pulsed magnetic field gradient applied along the z axis: G1 = (0.5 ms, 15 G/cm). (c) ^{1}H-^{15}N HSQC (left) and ^{15}N-selective HSFPT ^{1}H 1D (right) spectra of [Val-^{15}N] MBP. 1D slices of Val181, Val183, and Val261 extracted from the ^{1}H-^{15}N HSQC spectrum are shown for comparison. The carrier frequencies in the HSFPT spectra are set to 114.2 ppm for observing Val183, 123.2 ppm for observing Val181, and 129.0 ppm for observing Val261. The maximum t_1 ($t_{1,MAX}$) was set to 52.6 ms (top) or 13.2 ms (bottom), and the signal intensities were scaled in such a way that the total measurement time is equal to that of the HSFPT ^{1}H 1D spectra. (d) Comparison of the signal heights between the first slice of the HSQC (t_1 = 0) (black) and the ^{15}N-selective HSFPT ^{1}H 1D spectra observing Val183 (green) and Val261 (red). The numbers of scans are the same for these experiments. The [Val-^{15}N] MBP sample was used. (e) Plots of the theoretical values of S_{HSFPT}/S_{HSQC} as a function of the number of t_1 complex point or $t_{1,MAX}$, calculated with different effective relaxation rates. The increment in each t_1 complex point was set to 417 μs, which corresponds to the spectral width of 2400 Hz. (f) Plots of the intensities of the Val181 and Val183 signals as a function of the ^{15}N offset frequency. The apparent FWHM values are shown. Dots represent the experimentally observed values, and the lines represent the simulated curves obtained from the density matrix calculations.

at 20 °C ($\tau_c \sim 28$ ns), and found that we were able to selectively observe ^{1}H amide signals from restricted ^{15}N bandwidths in the ^{15}N-selective HSFPT ^{1}H 1D spectra (Fig. 2c).

We then compared the intrinsic sensitivities of these two schemes, by comparing the signal height of the first slice of ^{1}H-^{15}N HSQC ($t_1 = 0$) with those of the ^{15}N-selective HSFPT ^{1}H 1D spectra obtained with the same number of scans. We found that the signal heights were almost the same between them, reflecting the fact that the total magnetization transfer times are not very different between these two schemes (Fig. 2d). These results indicate that the intrinsic sensitivity of the ^{15}N-selectice HSFPT scheme is comparable to that of the ^{1}H-^{15}N HSQC. Although the intrinsic sensitivity of these two schemes was almost the same, when we compared the signal heights of the ^{15}N-selective HSFPT ^{1}H 1D spectra with the cross sections of the ^{1}H-^{15}N HSQC spectra, we could observe significant increases of 2.5- to 6-fold in the signal height in the ^{15}N-selective HSFPT ^{1}H 1D spectra, as compared to the ^{1}H-^{15}N HSQC spectrum recorded with the same measurement time (Fig. 2c). The increase in the signal height is attributed to the fact that the relaxation loss during the t_1 period is avoided in the HSFPT spectra, and this increase in the signal height strongly depends on the maximum length of the evolution period in the indirect dimension ($t_{1,MAX}$), which defines the resolution in the indirect dimension (Fig. 2c). We should note that the increase in the signal height also leads to the improvement in signal-to-noise ratio in the direct dimension (Fig. S5a). This is because the experimentally observed noise levels are similar in the direct dimension, when the 2D HSQC and 1D HSFPT spectra are recorded with the same measurement time and the same number of free induction decays are co-added.

We then quantitatively evaluated the increase in the signal height in the ^{15}N-selective HSFPT ^{1}H 1D spectra, as compared to the ^{1}H-^{15}N HSQC spectra. The signal height, S, of a discrete Fourier transformed spectrum can be represented by the following equations, assuming that M equidistant points between 0 and $t_{1,MAX}$ are sampled and n complex interferograms are co-added [2]. $s^e(t)$ represents an envelope function, which can be described with an effective relaxation rate $R_{2,eff}$ during the t_1 period.

$$S = n\sum_{k=0}^{M-1} s^e\left(k\frac{t_{1,MAX}}{M}\right) \tag{4}$$

$$s^e(t) = s^e(0)exp(-R_{2,eff}t) \tag{5}$$

In the indirect dimension of the ^{1}H-^{15}N HSQC spectrum, the signal height, S_{HSQC}, can be represented using the following equation.

$$S_{HSQC} = ns^e(0)\sum_{k=0}^{M-1}\exp\left(-R_{2,eff}k\frac{t_{1,MAX}}{M}\right) \tag{6}$$

In the case of the ^{15}N-selective HSFPT 1D spectrum, the signal height obtained with a single scan is almost equal to the s^e (0) of the HSQC, as mentioned above, and 2 nM scans can be co-added with the same measurement time. This is because the 2 components (*cosine* and *sine* components) per each complex point are recorded in the indirect dimension of the HSQC. Therefore, the signal height in the HSFPT spectrum, S_{HSFPT}, obtained with the same measurement time as that in the HSQC, can be represented by the following equation.

$$S_{HSFPT} = 2nMs^e(0) \tag{7}$$

In the case of the ^{1}H-^{15}N HSQC spectrum of [Val-^{15}N] MBP, the $R_{2,eff}$ rates of Val183 and Val261 were about 55 s^{-1} for both residues, as estimated from the signal decay in the t_1 period, and the values of $t_{1,MAX}$ and M were set to 52.6 ms and 128 points, respectively (Fig. S5c). By using these parameters, the increase in signal height in the HSFPT scheme, S_{HSFPT}/S_{HSQC}, can be calculated as 6.1, which is consistent with the experimentally observed increase in signal height. In these calculations, the contributions of the longitudinal relaxation, which can affect the initial equilibrium magnetization, were not taken into account, because the ^{1}H spin states at the beginning of the detection period were the same between these two schemes (in-phase H_y coherernce), and the difference in the longitudinal relaxation during the HSQC or HSFPT sequence was expected to be very small. Theoretically, under the same experimental conditions, the increase in the signal height in the HSFPT scheme is expected to be larger than 2.5-fold for proteins with molecular masses larger than 20 kDa, which roughly corresponds to the rotational correlation time of 10 ns [9,29]. The increase in the signal height is also dependent on the number of the t_1 complex point and $t_{1,MAX}$, because the relaxation loss during the t_1 frequency discrimination period can be partially prevented when we reduce the number of the complex point. Fig. 2e shows the plots of the theoretical values of S_{HSFPT}/S_{HSQC} as a function of the number of t_1 complex point or $t_{1,MAX}$, calculated with different effective relaxation rates. For example, under the conditions of the effective relaxation rates between 40 and 60 s^{-1}, the increase in signal height in the HSFPT scheme is expected to be over 3-fold as compared to the two-dimensional HSQC with the spectral resolution of 40 Hz ($t_{1,MAX}$ = 25 ms). These results indicate that the increase in the signal height in the HSFPT scheme would be relatively modest if we compromise the spectral resolution in 2D measurements, however, at least 2-fold increase in signal height is expected in the HSFPT scheme, which certainly represents a useful enhancement.

We also characterized the selectivity in the ^{15}N dimension, by recording the ^{15}N-selective HSFPT ^{1}H 1D spectra of Val181 and Val183 with different ^{15}N offset frequencies. Fig. 2f shows the plots of the signal heights as a function of the ^{15}N offset frequency. The apparent full widths at half maximum (FWHMs) were about 94 Hz in both cases, showing that we can separately observe the ^{15}N-selective HSFPT ^{1}H 1D spectra when the difference in the ^{15}N resonance frequency is larger than about 100 Hz. Considering the dispersion in the resonance frequencies of the amide ^{15}N, this bandwidth would be sufficient for selectively observing the amide signals of interest. In support of this notion, all of the Val amide signals could be resolved in the ^{15}N dimension in the ^{15}N-frequency-swept HSFPT ^{1}H 1D spectra of [Val-^{15}N] MBP (Fig. S6a).

2.3. Applications of the HSFPT scheme to the side-chain methyl $^1H_3$-^{13}C spin system

To directly observe high molecular weight proteins whose molecular mass is on the order of tens of thousands Daltons, it is particularly beneficial to observe the ^{1}H-^{13}C correlation in the side-chain methyl $^1H_3$-^{13}C spin system, because a large enhancement in the sensitivity can be achieved, derived from the methyl transverse relaxation-optimized spectroscopy (methyl-TROSY) effect [25,26]. In addition, the chemical shifts of the methyl carbons are well dispersed, reflecting the distributions of the side-chain rotamers [30–32], making it feasible to selectively observe the methyl signals that serve as sensitive probes by using the HSFPT scheme. Therefore, we set out to extend the application of the HSFPT scheme to the side-chain methyl $^1H_3$-^{13}C spin system. We applied the HSFPT scheme, which was established in the two-spin system, to the methyl $^1H_3$-^{13}C spin system of [2-^{13}C] sodium acetate (J = 127.1 [Hz]) (Fig. 3a). We then compared the results with those obtained using the INEPT scheme (Fig. 3b). We could observe the phase-inversion of the in-phase H_y coherence most efficiently when we used the CW field of 70–90 Hz and the total transfer time of 9–11 ms (Fig. S7a). Similar results were also

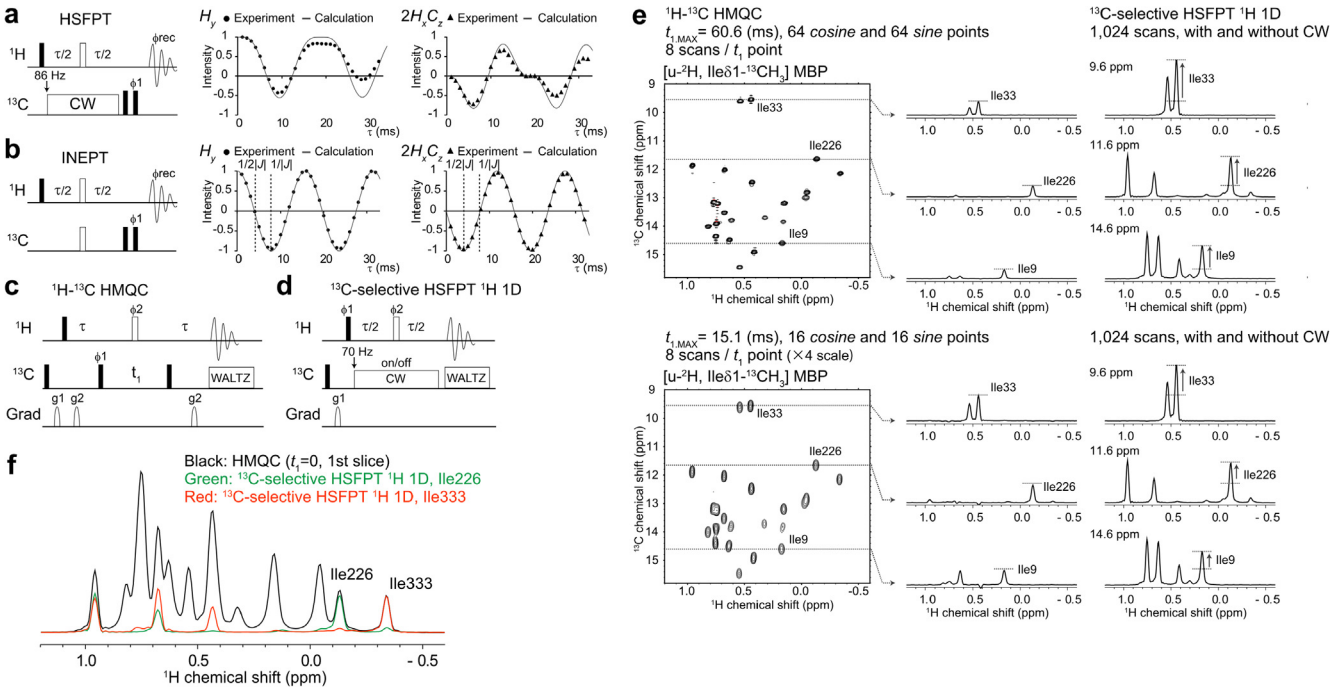

Fig. 3. Applications of the HSFPT scheme to the methyl $^{1}H_3$-^{13}C spin system. (a) The pulse sequence of the ^{13}C-selective HSFPT ^{1}H 1D with selective detections of the in-phase H_y and anti-phase $2H_xC_z$ coherences (left). The CW field strength was set to 86 Hz. Unless otherwise specified, pulse phases are along the $\times$ axis. The $\phi1$ and ϕrec phases are changed as described in Fig. 1a. Filled and open rectangles represent 90° and 180° pulses, respectively. Plots of the signal intensities observing the in-phase H_y or anti-phase $2H_xC_z$ coherences as a function of τ (right). The [2-^{13}C] sodium acetate sample was used. (b) The pulse sequence of the ^{13}C-edited INEPT ^{1}H 1D with selective detections of the in-phase H_y and anti-phase $2H_xC_z$ coherences (left). The $\phi1$ and ϕrec phases are changed as described in Fig. 1b. Plots of the signal intensities observing the in-phase H_y or anti-phase $2H_xC_z$ coherences as a function of τ (right). The [2-^{13}C] sodium acetate sample was used. (c) The pulse sequence of the ^{1}H-^{13}C HMQC [25]. The value of the INEPT transfer time τ is set to 3.9 ms. The ^{13}C decoupling during acquisition is achieved with a 3.3 kHz WALTZ16 field [92]. The following phase cycling scheme is used: $\phi1 = \{x, -x\}$; $\phi2 = \{2(x), 2(y), 2(-x), 2(-y)\}$; receiver = $\{x, -x, -x, x\}$. Quadrature detection is achieved via states-TPPI of phase $\phi1$ [91]. The duration and the amplitude of the sine-shaped pulsed magnetic field gradient applied along the z axis: G1 = (1 ms, 15 G/cm); G2 = (0.5 ms, 20 G/cm). (d) The pulse sequence of the ^{13}C-selective HSFPT ^{1}H 1D. The CW field strength is set to 70 Hz, and the value of the HSFPT transfer time τ is set to 11 ms. The following phase cycling scheme is used: $\phi1 = \{x, -x\}$; $\phi2 = \{2(x), 2(-x)\}$; receiver = $\{x, -x\}$. The duration and the amplitude of the sine-shaped pulsed magnetic field gradient applied along the z axis: G1 = (0.5 ms, 15 G/cm). The spectra are acquired alternately with or without the CW irradiation, and a difference spectrum between them is recorded. (e) ^{1}H-^{13}C HMQC (left) and ^{13}C-selective HSFPT ^{1}H 1D (right) spectra of [u-^{2}H, Ileδ1-$^{13}CH_3$] MBP. 1D slices of Ile9, Ile33, and Ile226 extracted from the ^{1}H-^{13}C HMQC spectrum are shown for comparison. The carrier frequencies in the HSFPT spectra were set to 9.6 ppm for observing Ile33, 11.6 ppm for observing Ile226, and 14.6 ppm for observing Ile9. The maximum t_1 ($t_{1,MAX}$) was set to 60.6 ms (top) or 15.1 ms (bottom), and the signal intensities were scaled in such a way that the total measurement time is equal to that of the HSFPT ^{1}H 1D spectra. (f) Comparison of the signal heights between the first slice of the HMQC ($t_1 = 0$) (black) and the ^{13}C-selective HSFPT ^{1}H 1D spectra observing Ile226 (green) and Ile333 (red). The numbers of scans are the same for these experiments. The [u-^{2}H, Ileδ1-$^{13}CH_3$] MBP sample was used.

obtained when we used the [u-^{2}H, Ileδ1-$^{13}CH_3$] MBP sample (τ_c ~ 65 ns at 4 °C) (Fig. S7b). These results agreed well with those expected from the formulation in the two-spin system, indicating that the HSFPT scheme can also be applied to the side-chain methyl $^{1}H_3$-^{13}C spin system.

The major difference between the methyl $^{1}H_3$-^{13}C four-spin and ^{1}H-^{13}C two-spin systems is that the maximum transfer efficiency is lower in the methyl $^{1}H_3$-^{13}C spin system. In the methyl $^{1}H_3$-^{13}C spin system, a maximum of 75% of the initial in-phase magnetization could be phase-inverted, in contrast to the result that almost all of the initial in-phase magnetization could be phase-inverted in the two-spin system (Figs. 3a, S2, and S7). In order to examine the cause underlying this difference, we conducted density matrix calculations using the bases of the eigenfunctions for the methyl $^{1}H_3$-^{13}C spin system introduced by Kay and co-workers [26]. Our density matrix calculations showed that the transitions involving the outer energy levels of the spin 3/2 manifold do not efficiently evolve during the on-resonance ^{13}C CW irradiation, which prevents the transfer of the ^{1}H polarization to ^{13}C at the maximum efficiency. Since these outer transitions correspond to the outer lines of the methyl ^{13}C quartet, they efficiently evolve when ^{13}C CW is irradiated with about $\pm J$ Hz offset from the ^{13}C resonance frequency, resulting in a broad ^{13}C offset profile as compared to the two-spin system (Fig. S8a). In high molecular weight proteins, the relaxation rates of these outer transitions are very large, due to the intra-methyl dipolar interactions, and hence rapidly diminish before the detection period [25]. Therefore, we can safely neglect the contributions from these transitions and observe a sharp offset profile similar to that obtained in the two-spin system (Fig. S8b).

We then observed the ^{1}H-^{13}C HMQC and ^{13}C-selective HSFPT ^{1}H 1D spectra of [u-^{2}H, Ileδ1-$^{13}CH_3$] MBP at 4 °C (τ_c ~ 65 ns), and compared the signal heights between them, and found that we were able to selectively observe the ^{1}H methyl signals from the restricted ^{13}C bandwidths (Fig. 3c–e). We then compared the intrinsic sensitivities of these two schemes, by comparing the signal height of the first slice of ^{1}H-^{13}C HMQC ($t_1 = 0$) with those of the ^{13}C-selective HSFPT ^{1}H 1D spectra obtained with the same number of scans, and found that the intrinsic sensitivities of these two schemes were almost the same (Fig. 3f). When we compared the signal heights of the ^{13}C-selective HSFPT ^{1}H 1D spectra with the cross sections of the ^{1}H-^{13}C HMQC spectra, we could observe significant increases in the signal height of 2.2- to 4-fold in the ^{13}C- selective ^{1}H 1D spectra, as compared to the ^{1}H-^{13}C HMQC spectrum, depending on the $t_{1,MAX}$. Also, we were able to observe marked increase in the signal-to-noise ratio in the direct dimen-

sion (Fig. S5b). It should be noted that, in the HSFPT scheme, only the ^{13}C nuclei are irradiated and the mixing of the slow and fast relaxing transitions is minimal. Therefore, the HSFPT scheme can benefit from the methyl-TROSY effect similarly as in the case of the HMQC scheme, and can be effectively applied to high molecular weight proteins.

We also characterized the selectivity in the ^{13}C dimension, by recording the ^{13}C-selective HSFPT ^{1}H 1D spectra with different ^{13}C offset frequencies. The apparent FWHMs were about 92 Hz when using the CW field of 70 Hz and the transfer time of 11 ms (Fig. S8b). In the ^{13}C-frequency-swept ^{1}H 1D spectrum of MBP recorded with the static magnetic field strength of 14.1 Tesla (600 MHz ^{1}H frequency), we could not separately observe some Ile methyl signals in a crowded region. However, we were able to resolve these signals with the static magnetic field strength of 22.3 Tesla (950 MHz ^{1}H frequency), reflecting that the difference in the resonance frequency linearly increases with the static magnetic field strength (Fig. S6b). These results support the utility of the ultra-high field NMR and the feasibility of applying this scheme to the side-chain methyl groups in high molecular weight proteins.

2.4. Applications of the HSFPT scheme to relaxation experiments

We applied the selective HSFPT scheme to relaxation experiments, to maximize the sensitivities. We designed the CPMG RD and CEST experiments with ^{15}N- or ^{13}C-selective observations, by either replacing the INEPT sequence with that of the HSFPT, or simply adding the ^{15}N- or ^{13}C-selective HSFPT sequence just before the detection period. Fig. 4a shows the pulse sequences for a ^{13}C-selective HSFPT ^{13}C single quantum (SQ) CPMG RD experiment, based on the reported 2D version of the sequence [33]. As compared to the 2D version of the sequence, the forward and reverse INEPT blocks were replaced with the HSFPT sequences using the CW field of 90 Hz and the transfer time of 6 ms, and the t_1 frequency discrimination period was removed. We tested this sequence using the [u-^{2}H, Ileδ1, Leuδ2, Valγ2-$^{13}CH_3$] T4 lysozyme mutant ($\tau_c \sim 30$ ns at 4 °C), which exists in a two-state exchange process with an exchange rate (k_{ex}) of about 610 s^{-1} [34,35] (Fig. 4b), and confirmed that accurate exchange parameters could be obtained by fitting the dispersion curves (Fig. 4c). We should note that substantial increases in the signal height up to 3.4-fold were observed, and the errors in the dispersion profiles significantly decreased with the HSFPT scheme.

We also designed the pulse sequences of ^{15}N SQ CPMG RD [36], ^{1}H SQ CPMG RD [37], and ^{15}N CEST [13] with ^{15}N-selective observations for the ^{1}H-^{15}N two-spin system (Figs. S9 and S10); and ^{1}H-^{13}C multiple quantum (MQ) CPMG RD [38] and ^{13}C CEST [39] with ^{13}C-selective observations for the methyl $^{1}H_3$-^{13}C spin system (Figs. 5a and S11), based on the reported 2D versions of the sequences. By applying these sequences to the FF domain [40,41] and the T4 lysozyme mutant [34], we confirmed that the microsecond-to-millisecond conformational exchange processes could be characterized with sufficient accuracy and improved sensitivity per unit of time. We should add that, in the applications to the ^{1}H-based relaxation analyses (^{1}H SQ CPMG RD and ^{1}H-^{13}C MQ CPMG RD), signal artifacts were observed by simply replacing the INEPT sequence with that of the HSFPT, because the magnetization transfer pathways were less rigorously selected in these ^{1}H-based experiments (Fig. S12). In these cases, we could efficiently remove these artifacts by adding the whole $^{15}N/^{13}C$-edit ^{1}H 1D HSFPT sequence just before the detection period instead of replacing the INEPT sequence to that of the HSFPT (Fig. 5a and S9b).

2.5. Comparisons with other selective polarization transfer experiments.

We compared the sensitivity and selectivity of the HSFPT scheme with those obtained with other selective coherence transfer schemes. In this section, we will mainly focus on the comparison with the selective cross polarization (CP) scheme, in which the weak spin-lock fields are simultaneously applied to both scalar-coupled nuclei to transfer the polarization, based on the previous report that the selective CP scheme showed superior sensitivity and selectivity to those obtained with selective INEPT or selective excitation schemes [19,20,24].

We first compared the signal height of the HSFPT scheme with that of the selective CP scheme in the ^{1}H-^{15}N two-spin system (Fig. S13a). Fig. S13b shows the comparisons between the ^{15}N-selective ^{1}H 1D spectra obtained with the HSFPT and the selective CP schemes. Although both schemes exhibited similar signal sensitivities for [indole-^{15}N] DL-Tryptophan, the HSFPT scheme exhibited about a 1.8-fold higher signal height for [^{15}N-Val] MBP ($\tau_c \sim 28$ ns at 20 °C) than that obtained with the selective CP scheme. This is because the HSFPT scheme requires a shorter transfer time than the selective CP scheme (total 12 ms in the HSFPT vs. 21.6 ms in the selective CP), and hence the relaxation loss is smaller in the HSFPT scheme. These results support the notion that the HSFPT scheme is more beneficial in applications to the ^{1}H-^{15}N two-spin systems of high molecular weight proteins, as compared to the selective CP scheme.

We also compared the sensitivities in the methyl $^{1}H_3$-^{13}C spin system, and demonstrated that the HSFPT scheme exhibited about 3.7-fold higher signal height than that obtained with the selective CP scheme (Figs. S13c and d). Notably, we could observe an increase in the signal height by using the HSFPT scheme, although the transfer time of the HSFPT scheme was not much different from that of the selective CP scheme in the methyl $^{1}H_3$-^{13}C spin system (total 9 ms in the HSFPT vs. 10.6 ms in the selective CP), and the increase in the signal height was commonly observed for both [2-^{13}C] sodium acetate and [u-^{2}H, Ileδ1-$^{13}CH_3$] MBP ($\tau_c \sim 65$ ns at 4 °C). Our density matrix calculations showed that, in the selective CP scheme, the initial in-phase H_x coherence was converted to the in-phase $0.29 \times C_x$ coherence, whereas the initial in-phase H_x coherence was converted to the anti-phase $0.84 \times 2C_zH_y$ in the HSFPT scheme. These results indicate that the polarization transfer efficiency is intrinsically low in the methyl $^{1}H_3$-^{13}C spin system, which is in contrast to the result that almost complete polarization transfer from the initial in-phase H_x to the in-phase N_x can be achieved in the ^{1}H-^{15}N two-spin system, if the relaxation loss is not considered (Fig. S13e). From these results, we concluded the HSFPT scheme shows superior performance in sensitivity, not only with high molecular weight proteins but also with smaller ones. It should also be noted that the continuous irradiations on ^{1}H can lead to the mixing of the slow and fast relaxing transitions and hence accelerate the relaxation loss during the transfer period, further supporting the effectiveness of the HSFPT scheme, especially in the methyl $^{1}H_3$-^{13}C spin systems of high molecular weight proteins.

Second, we compared the selectivity of the HSFPT scheme with that of the selective CP scheme. We measured the ^{15}N- or ^{13}C-frequency-swept spectra and compared the FWHMs between these two schemes. In the ^{1}H-^{15}N two-spin system, the apparent FWHM in the HSFPT scheme was about 94 Hz with the CW field of 50 Hz and the transfer time of 12 ms, as shown in the ^{15}N-frequency-swept spectra of [^{15}N-indole] DL-Tryptophan (Fig. S13f). In contrast, the apparent FWHM in the selective CP was about 42 Hz with the spin lock field of 40 Hz and the transfer time of 10.8 ms, which were nearly the optimal conditions for the

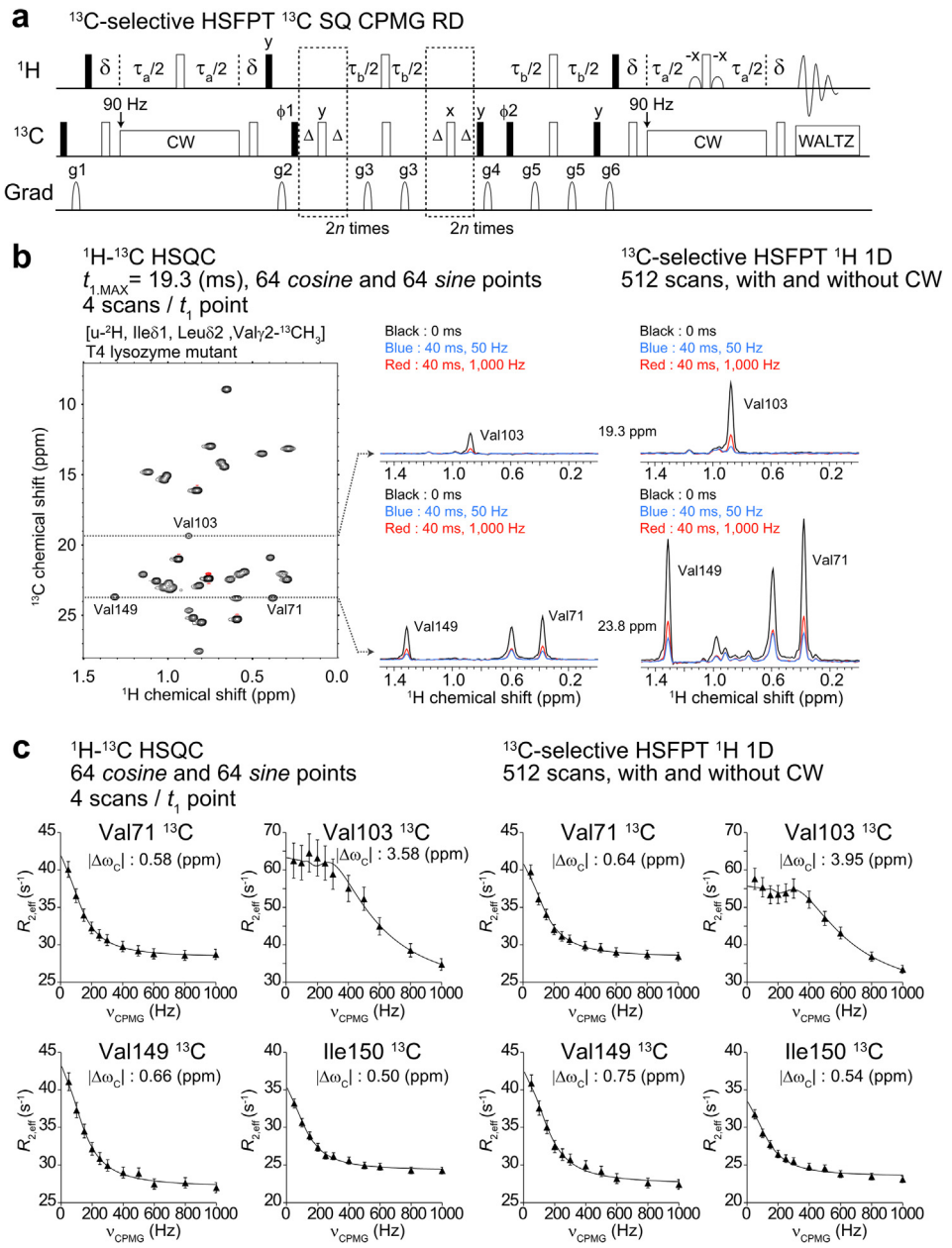

Fig. 4. ^{13}C SQ CPMG RD experiment with the HSFPT scheme. (a) The pulse sequence of the ^{13}C-selective HSFPT ^{13}C SQ CPMG RD experiment. Unless otherwise specified, pulse phases are along the $\times$ axis. Filled and open rectangles represent 90° and 180° pulses, respectively. Open shapes represent water selective 90° pulses. The CW field strength is set to 90 Hz, and the value of the HSFPT transfer time τ_a is set to 6 ms. The value of the delay τ_b is set to 4 ms. δ denotes a short-delay for power-switching. The ^{13}C decoupling during acquisition is achieved with a 3.3 kHz WALTZ16 field [92]. The following phase cycling scheme is used: $\phi1 = \{x, -x\}$; $\phi2 = \{2(x), 2(-x)\}$; receiver = $\{x, -x, -x, x\}$. The duration and the amplitude of the sine-shaped pulsed magnetic field gradient applied along the z axis: G1 = (0.5 ms, 4 G/cm); G2 = (1 ms, 25 G/cm); G3 = (0.3 ms, 12 G/cm); G4 = (0.5 ms, 8 G/cm); G5 = (0.3 ms, −10 G/cm); G6 = (0.7 ms, 8 G/cm). (b) ^{1}H-^{13}C HSQC spectrum of [u-^{2}H, Ileδ1, Leuδ2, Valγ2-^{13}CH$_3$] T4 lysozyme mutant and 1D slices of Val71, Val103, and Val149 extracted from the 2D ^{13}C SQ CPMG RD spectra are shown [33] (left). The 1D spectra of ^{13}C-selective HSFPT ^{13}C SQ CPMG RD experiments observing Val71, Val103, and Val149 are shown for comparison (right). The results of the reference (black), ν_{CPMG} = 50 Hz (blue), and ν_{CPMG} = 1,000 Hz (red) are overlaid. (c) ^{13}C SQ CPMG RD curves of Val71, Val103, Val149, and Ile150 obtained from the 2D experiments (left), and the 1D HSFPT experiments (right).

selective CP transfer (the spin lock field of $\sqrt{3}|J|/4$ Hz and the transfer time of $1/|J|$). A comparison of these two results indicated that the selective CP could achieve about 2.2-fold better selectivity in the ^{15}N dimension, owing to the use of the weaker CW field and the longer transfer time. However, under these conditions, relatively large sidebands were observed in the selective CP experiment, which were caused by off-resonance dips observed at around $\pm J$ Hz in the excitation profile [20]. In order to obtain a clean excitation profile in the selective CP scheme, the stronger spin lock field of 70 Hz, which roughly corresponds to $3|J|/4$ Hz, should be used. Under these conditions, the apparent FWHM in the selective CP scheme was about 77 Hz, which was comparable to that obtained with the HSFPT scheme. In the methyl ^{1}H$_3$-^{13}C spin system, the selectivity in the ^{13}C dimension was comparable between these two schemes, as demonstrated by the results that the FWHMs in these two schemes were almost the same in the ^{13}C-frequency-swept spectra of [u-^{2}H, Ileδ1-^{13}CH$_3$] MBP (Fig. S13g). This is because the strength of the CW field and the transfer time are nearly the same in both the selective CP and HSFPT schemes.

Collectively, we concluded that, as compared to the selective CP scheme, the HSFPT scheme shows better performance in sensitivity and a comparable selectivity under practical conditions in both the ^{1}H-^{15}N and methyl $^{1}H_3$-^{13}C spin systems of high molecular weight proteins. The loss of sensitivity is one of the critical factors limiting the applications of NMR to high molecular weight proteins; therefore, the sensitivity gain in the HSFPT scheme is a major advantage over the selective CP and other selective polarization transfer schemes. However, when we consider the applications to relaxation experiments, the selective CP has still a big advantage over the HSFPT scheme that the selective CP results in the in-phase ^{15}N or ^{13}C coherence, which has a favorable relaxation property as compared to the anti-phase coherence. Therefore, the selective CP is sometimes preferred for relaxation measurements in the applications to the ^{1}H-^{15}N or ^{1}H-^{13}C two spin system, and the application of the HSFPT is beneficial especially in the applications to the methyl $^{1}H_3$-^{13}C spin system, where the selective CP is not very efficient.

2.6. Applications of the HSFPT scheme to a high molecular weight membrane protein, KirBac1.1

To demonstrate the effectiveness of the HSFPT scheme, we applied the scheme to the membrane protein KirBac1.1, which has an apparent molecular mass of over 200 kDa as a tetramer in detergent micelles [42,43]. KirBac1.1 is a prokaryotic homologue of an inwardly rectifying potassium channel in eukaryotes, and $^{86}Rb^{+}$ intake assays and electrophysiological analyses of KirBac1.1 have shown that the channel exhibits a basal K^{+}-permeation activity in the absence of ligands [44–46]. Although the crystal structure of KirBac1.1 has been solved, the K^{+}-permeation gate located in the transmembrane (TM) region adopted a closed conformation, and therefore the molecular mechanism for the basal K^{+}-permeability of the channel has remained unclear. Previously, we have shown that the TM region exists in a conformational exchange process on the microsecond to millisecond time scale, and proposed that the conformational plasticity of the TM region is responsible for the basal K^{+}-permeability [47]. However, quantitative evaluations of the exchange process were quite difficult, due to the protein's large molecular weight.

To quantitatively characterize the conformational dynamics of the TM gate, we conducted the ^{1}H-^{13}C MQ CPMG RD experiment with the HSFPT scheme on [u-^{2}H, Ileδ1-$^{13}CH_3$] KirBac1.1 in *n*-dodecyl-β-D-maltopyranoside (DDM) micelles. The protein has an apparent molecular mass of about 220 kDa, assuming the DDM micelle size of 72 kDa (Fig. 5b). We set the ^{13}C frequency on-resonance to the Ile138 residue (^{13}C 12.9 ppm), which exhibited a significant exchange contribution in our previous analyses [47]. Under these conditions, we could simultaneously observe the Ile89 signal, with a ^{13}C chemical shift similar to that of Ile138. Fig. 5b shows the comparisons of the signal sensitivities between the HSFPT scheme and the reported 2D HMQC-based scheme, which clearly indicated that a significant increase in the signal height, up to 4-fold, was achieved by incorporating the HSFPT scheme. Thanks to the increase in the sensitivity, we were able to detect a large dispersion for Ile138, as well as a small but significant dispersion for Ile89 (Fig. 5c). By fitting the dispersion curves to the theoretical formula assuming a global two-state exchange [38], we obtained the exchange rate of $920 \pm 260\ s^{-1}$ and the minor state population of 11 ± 7%. The obtained chemical shift differences were larger in the ^{13}C direction than the ^{1}H direction for both residues, consistent with our previous results that the exchange contributions for the differential MQ relaxation rates were relatively small and the ^{1}H chemical shift differences were expected to be small for both residues [47]. From the peak shift analysis between the ^{1}H-^{13}C HSQC and HMQC spectra [48] (Fig. S14a), we estimated the population of the major state with the lower field value of the ^{13}C chemical shift (L state) to be 89%, and the minor state with the higher field value of the ^{13}C chemical shift (H state) to be 11%. Using these k_{ex} and population values, the lifetimes of the L and H states were estimated to be 9.6 ms and 1.2 ms, respectively. These values are reasonably consistent with the single channel behaviors of KirBac1.1, in which the duration times of the different K^{+}-conducting states are on the order of 1 to 100 ms [46], supporting our proposal that the observed conformational exchange process is closely related to the regulation of the K^{+}-permeation.

To further investigate the functional implications of the observed exchange process, we analyzed a mutant with the substitution of a positively charged residue located on the membrane interface, Arg148, which forms intra-subunit interactions between the transmembrane helices. We conducted $^{86}Rb^{+}$ intake assays to evaluate the K^{+}-permeability, and found that the R148K mutant exhibited higher K^{+}-permeability than that of the wild type (Fig. S14b). We then measured the ^{1}H-^{13}C HMQC spectrum of the R148K mutant, and found that the Ile138 signal was split into two signals, with chemical shifts roughly corresponding to those of the H and L states in the wild type (Figs. S14c and d). These observations strongly suggested that the R148K mutant exists in a similar conformational equilibrium to that observed in the wild type, and the exchange rate between these two states is slowed down in the R148K mutant. The two Ile138 signals in the R148K exhibited the similar signal intensities, reflecting the fact that the H and L states are nearly equally populated in the mutant, and that the population of the H state is significantly higher than that in the wild type. Together with the results of the $^{86}Rb^{+}$ intake assays, we presumed that the H state is responsible for the high K^{+}-permeability.

To further validate this model, we conducted molecular dynamics simulations to evaluate the rotameric state of Ile138. The ^{13}C chemical shifts of the Ileδ1 methyl carbon reflect the distributions of the side-chain χ_2 angles (*gauche*-: 9.3 ppm, *trans*: 14.8 ppm), and the higher filed value of the ^{13}C chemical shift indicates that the fraction of the *gauche*- conformation is increased [31]. We used two coordinates as the initial structures, the crystal structure of KirBac1.1 in which the transmembrane K^{+}-gate adopts the closed conformation and Ile138 adopts a *trans* rotamer (closed structure), and the homology model constructed from the crystal structure of the KirBac3.1 S129R mutant, in which the K^{+}-gate adopts the open conformation (open structure) [49] (Fig. S14e). During the 20 ns simulation using the closed structure, the side chain of Ile138 mainly adopted the *trans* rotamer, because the formation of the *gauche*- rotamer was prevented by the steric hindrance with the side-chain of Met135 (Figs. S14e and f). In contrast, during the simulation using the open structure, the Ile138 side chain adopted both the *trans* and *gauche*- rotamers to similar extents, because the orientation of the transmembrane helix was changed and fewer van-der-Waals contacts were formed in the open structure. We calculated the fractions of the *gauche*- rotamer from the 20 ns trajectories, and found that the fraction of the *gauche*- rotamer in the open structure (55%) was significantly larger than that in the closed structure (11%) (Fig. S14f). These results also support our notation that the H state, defined in the NMR analyses represents the conformation, which is responsible for the high K^{+}-permeability.

To confirm that the observed conformational exchange process in the DDM micelles reflects that in a native membrane environment, we conducted ^{1}H-^{13}C MQ CPMG RD experiments using [u-^{2}H, Ileδ1-$^{13}CH_3$] KirBac1.1 reconstituted into nanodiscs (KirBac-nanodiscs), which closely mimic KirBac1.1 in the native membrane environment [50,51] (Fig. S14g). Despite the lower sample concentration and the increased apparent molecular mass

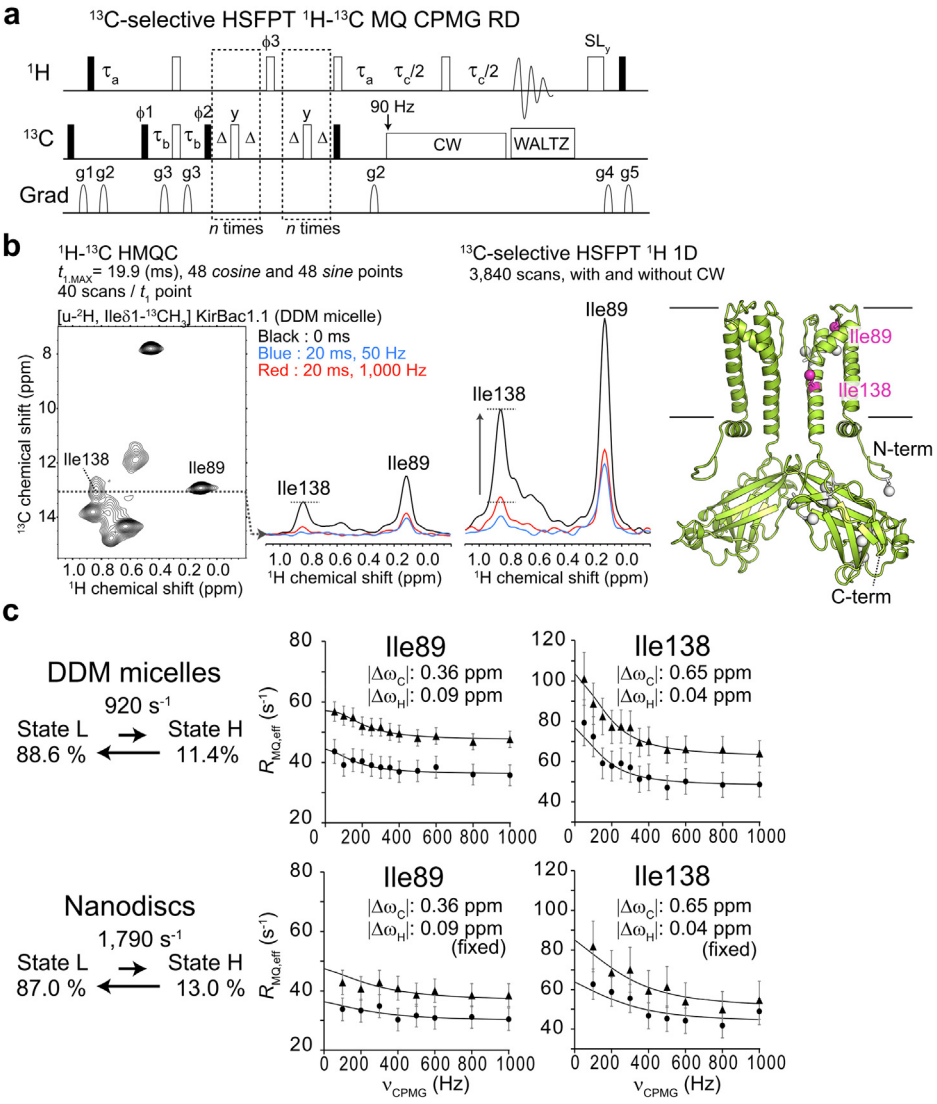

Fig. 5. ^{1}H-^{13}C MQ CPMG RD experiments of KirBac1.1 with the HSFPT scheme. (a) The pulse sequence of the ^{13}C-selective HSFPT ^{1}H-^{13}C MQ CPMG RD experiment. Unless otherwise specified, pulse phases are along the × axis. Filled and open rectangles represent 90° and 180° pulses, respectively. The values of the delays τ_a and τ_b are set to 3.4 and 1.0 ms, respectively. The CW field strength is set to 90 Hz, and the value of the HSFPT transfer time τ_c is set to 8 ms. The ^{13}C decoupling during acquisition is achieved with a 3.3–3.6 kHz WALTZ16 field [92]. A 40 ms ^{1}H spin-lock field (10 kHz, y axis) is applied after acquisition (SL_y), which eliminates the transverse components of magnetization [93]. The following phase cycling scheme is used: $\phi1 = \{x, -x\}$; $\phi2 = \{2(y), 2(-y)\}$; $\phi3 = \{4(x), 4(y)\}$; receiver = $\{x, -x, x, -x, -x, x, -x, x\}$. The duration and the amplitude of the sine-shaped pulsed magnetic field gradient applied along the z axis: G1 = (1 ms, 5 G/cm); G2 = (0.6 ms, 20 G/cm); G3 = (0.2 ms, −20 G/cm); G4 = (1.2 ms, −24 G/cm); G5 = (0.6 ms, −24 G/cm). The spectra with or without the CW irradiation are acquired alternately, and a difference spectrum between them is recorded. (b) ^{1}H-^{13}C HMQC spectrum of [u-^{2}H, Ileδ1-^{13}CH$_3$] KirBac1.1 in the DDM micelles, and 1D slices of Ile89 and Ile138 extracted from the 2D ^{1}H-^{13}C MQ CPMG RD spectra are shown [38] (left). The 1D spectra of ^{13}C-selective HSFPT ^{1}H-^{13}C MQ CPMG RD experiments observing Ile89 and Ile138 are shown for comparison (right). The results of the reference (black), ν_{CPMG} = 50 Hz (blue), and ν_{CPMG} = 1,000 Hz (red) are overlaid. The mapping of Ile89 and Ile138 on the crystal structure of KirBac1.1 is shown (PDB ID: 1P7B)[43]. Only two facing subunits of the tetramer are shown for clarity. (c) ^{1}H-^{13}C MQ CPMG RD curves of Ile89 and Ile138 obtained from the 1D HSFPT experiments. The results obtained with KirBac1.1 in the DDM micelles are shown on the left, and those obtained with KirBac1.1-nanodiscs are shown on the right.

of the KirBac-nanodiscs, which was estimated to be about 300 kDa [52], we were able to obtain dispersion curves by utilizing the HSFPT scheme (Fig. 5c). If we assumed that the ^{13}C and ^{1}H chemical shift differences between the two states were the same in the DDM micelles and in the nanodiscs, then we could obtain the exchange rate of 1790 ± 530 s^{-1} and the minor state population of 13 ± 3% in the nanodiscs. We found that the relative populations of the two states were nearly the same in the DDM micelles and nanodiscs. The small difference in the exchange rate probably reflects the fact that the structure of the transition state between the two exchanging states is slightly stabilized by ~0.4 kcal/mol in the membrane environment.

Taken together, these results demonstrate that the conformational exchange process of the TM region is closely related to the regulation of the K^+-permeability across the membrane, and the shift in the relative populations of the two states is the underlying mechanism for the increased K^+-permeability in the R148K mutant.

3. Discussion

In this study, we developed the HSFPT scheme, which enables us to selectively observe the ^{1}H nuclei bonded to the ^{13}C or ^{15}N

nuclei, with specified resonance frequencies. We demonstrated that ^{15}N- or ^{13}C-selective ^{1}H HSFPT spectra can be obtained in the ^{1}H-^{15}N and methyl $^{1}H_3$-^{13}C spin systems in high molecular weight proteins, and a significant improvement in the sensitivity per unit of time can be achieved by avoiding the relaxation loss during the frequency discrimination period. We also applied the HSFPT scheme to the CPMG RD and CEST experiments. The effectiveness of the scheme was demonstrated in the applications to KirBac1.1 in both detergent micelles and a reconstituted membrane environment, corresponding to the apparent molecular weights of 220 K and 300 K, respectively. We revealed that the TM region forming the K^+-gate exists in a conformational exchange process that is closely linked to the regulation of the K^+-permeability across the membrane.

Although we have mainly focused on the improvement in sensitivity so far, we should note that the scheme also greatly improves the time resolution in applications to real-time NMR [53], when the signals of interest are unresolved in the ^{1}H dimension. Under the white Gaussian noise assumption, the n-times gain in sensitivity results in n^2-times improvement in the time resolution with the same sensitivity, making it possible to characterize faster kinetic processes and/or obtain accurate kinetic parameters with the HSFPT scheme. It should also be noted that the HSFPT ^{1}H 1D measurement requires a minimum of two scans to measure one 1D spectrum, therefore the incorporation of the HSFPT scheme would also help in reducing the sampling intervals. Furthermore, the HSFPT would be also useful for the analyses of spin connectivity, by incorporating the selective off-resonance methods such as CODED and spin-state selective off-resonance decoupling (SITAR) [54–56].

When we consider net coherence transfer efficiency from the in-phase H_y coherence to the anti-phase $2H_xN_z/2H_xC_z$ coherence, the transfer efficiency is usually lower in the HSFPT scheme than in the INEPT scheme, because the transfer time is longer in the HSFPT scheme (9.9 ms in the HSFPT and 5.6 ms in the INEPT for the ^{1}H-^{15}N spin system, and 6.0 ms in the HSFPT and 3.9 ms in the INEPT for the $^{1}H_3$-^{13}C methyl spin system). Thus, the increase in the signal height in the HSFPT scheme is achieved solely by avoiding the relaxation loss in the frequency discrimination period, which compensates the lower transfer efficiency of the HSFPT scheme. When we compare the coherence transfer efficiency with other transfer schemes in the case of highly deuterated proteins, the transfer efficiency is expected to be lower in the HSFPT scheme as compared to the relaxation optimized coherence transfer schemes, such as TROSY [57], cross-correlated relaxation-induced polarization transfer (CRIPT), cross-correlated relaxation-enhanced polarization transfer (CRINEPT) [58,59], polychromatic selective polarization inversion (PC-SPI) [60], and the other optimally designed coherence transfer schemes utilizing optimal control theory [61–63]. However, the HSFPT scheme enables us to observe the ^{1}H NMR signals from the restricted ^{15}N-bandwidth, hence the scheme is quite advantageous when the ^{15}N resonance frequency of the signal of interest is available. In addition, we should note that these relaxation optimized sequences have been focused on the main-chain ^{1}H-^{15}N and aromatic side-chain ^{1}H-^{13}C two-spin systems, and the coherence transfer scheme that can be applied to the $^{1}H_3$-^{13}C methyl spin system has not been well established so far. Since methyl groups are highly sensitive and exhibit favorable relaxation properties in high molecular proteins, the HSFPT would be quite beneficial in the applications to high molecular weight proteins with molecular masses on the order of hundreds of kDa.

Liu and Prestegard have developed MD-DIRECT, in which NMR signals from a restricted ^{15}N-bandwidth can be recorded without coherence transfer by utilizing a ^{15}N/^{13}C frequency selective decoupling [64]. The higher signal sensitivity can be achieved in the MD-DIRECT method as compared to the HSFPT scheme in ultra-high molecular weight proteins, because the MD-DIRECT scheme is completely free from sensitivity losses during the coherence transfer period. However, the HSFPT is still advantageous in some points. First, the NMR signals obtained with the HSFPT scheme exhibit singlet line-shape, which is in contrast to the MD-DIRECT scheme which results in a triplet line-shape with central and outer lines of opposite phase. The single line-shape is better suited for quantitative analyses as compared to the triplet line-shape, especially when multiple signals are observed and degenerated in the ^{1}H dimension. Second, the selectivity in the ^{15}N/^{13}C frequency is higher in the HSFPT, because we can use weaker radio frequency fields in the HSFPT scheme than in the MD-DIRECT method.

One of the major drawbacks of the HSFPT scheme is that the information of the resonance frequencies must be used. For example, in the CPMG RD experiments using the HSFPT scheme, we have to know the resonance frequencies of the signals that exhibit significant dispersions in advance. This application is apparently unrealistic; however, it is usually easy to roughly estimate the exchange contributions by recording several ν_{CPMG} points, or by simply measuring the transverse relaxation rates. In addition, the numbers of signals that show significant exchange contributions are very limited in many cases [65–67]. Therefore, an effective approach would be to first identify the feasible candidates for the selective observation, and then observe these signals with improved sensitivity by using the HSFPT scheme. Another drawback is that the HSFPT scheme is relatively susceptible to the artefacts originating from the strong nearby signals, or signals from unwanted magnetization transfer pathways. This is because the Fourier transformation is not performed in the indirect dimension, which usually shifts these artefacts to the centers or edges of the spectral window. Therefore, care should be taken to avoid observing these artefacts, especially when the signal of interest is located in a crowded region.

In conclusion, we established the HSFPT scheme that enables us to selectively observe the ^{1}H nuclei bonded to ^{13}C or ^{15}N nuclei with specified resonance frequencies. By utilizing the HSFPT scheme, we achieved significant improvements in the sensitivity as compared to the conventional 2D experiments based on the INEPT scheme, in the applications to high molecular weight proteins. Most multidimensional NMR experiments exploit the INEPT transfer scheme, and the INEPT block can be relatively easily replaced with the HSFPT block, therefore the HSFPT scheme can be similarly incorporated into other types of NMR experiments, such as R_1, R_2, ZZ-exchange [68], and heteronuclear-edited NOESY experiments, in a similar way as we demonstrated in the applications to the CPMG RD and CEST experiments. From these viewpoints, the HSFPT scheme would serve as a general scheme in biomolecular applications of NMR, and would further facilitate the investigations of structural dynamics of biologically important proteins with high molecular weights, which have been difficult to analyze by conventional NMR methodologies.

4. Methods

4.1. Sample preparations

The [^{15}N-indole] DL-Tryptophan (CIL) was dissolved in 90% H_2O and 10% D_2O solution at a concentration of 20 mM. The [ring-2-^{13}C] L-Histidine (CIL) was dissolved in 99% D_2O solution at a concentration of 20 mM. The [2-^{13}C] sodium acetate (CIL) was dissolved in 99% D_2O solution at a concentration of 50 mM.

The *E. coli* MBP (residues 1–370) protein was expressed in *E. coli* cells. For ^{15}N-Valine labeling, the plasmid encoding MBP was trans-

formed into *E. coli* ML24 cells (Addgene bacterial strain #61915) [69,70], and the cells were grown in M9 medium supplemented with 50 mg/L ^{15}N-Valine and other non-labeled essential amino acids. For methyl selective labeling, the plasmid encoding MBP was transformed into *E. coli* BL21-CodonPlus(DE3)-RP cells (Agilent Technologies). The cells were grown in deuterated M9 medium, and 50 mg/L of [methyl-^{13}C,3,3-$^{2}H_2$]-α-ketobutyric acid (for Ileδ1) was added 1 h prior to the induction [71]. The proteins were purified sequentially with Q sepharose (GE) and Amylose Resin (New England Biolabs), as described previously [47]. The NMR sample consisted of 0.5–0.8 mM MBP, 2 mM β-cyclodextrin, 20 mM sodium phosphate buffer (pH 7.2), 3 mM NaN_3, and 0.1 mM EDTA, in 10% D_2O (for [^{15}N-Val] MBP) or 99% D_2O (for [u-^{2}H, Ileδ1-$^{13}CH_3$] MBP).

The C54T, C97A, L99A, G113A, R119P T4 lysozyme mutant (residues 1–164) was expressed in *E. coli* BL21-CodonPlus(DE3)-RP cells (Agilent Technologies). For methyl selective labeling, the cells were grown in deuterated M9 medium, and 50 mg/L of [methyl-^{13}C, 3-$^{2}H_2$]-α-ketobutyric acid (for Ileδ1) (CIL) and 300 mg/L of [2-methyl ^{13}C, 4-$^{2}H_3$]-acetolactate (for Leuδ2 and Valγ2) (NMR-Bio) were both added 1 h prior to the induction [71,72]. The protein was purified sequentially on Hitrap SP (GE) and 26/60 Superdex 75 pg (GE) column, as described previously [34,35,73]. The NMR sample consisted of 1.2 mM T4 lysozyme mutant, 50 mM sodium phosphate buffer (pH 5.5), 25 mM NaCl, 3 mM NaN_3, and 2 mM EDTA in 99% D_2O.

The HYPA/FBP11 FF domain (residues 250–319), including an N-terminal GST-tag, was expressed in *E. coli* BL21-CodonPlus (DE3)-RP cells (Agilent Technologies) and purified as described previously [41,47]. The protein was first purified with Glutathione sepharose (GE). After the cleavage of the GST-tag with thrombin (Sigma-Aldrich), the FF domain was further purified using a Hitrap SP column (GE). The NMR sample consisted of 0.6–1.0 mM FF domain, 20 mM potassium phosphate buffer (pH 6.8), 50 mM NaCl, 0.2 mM NaN_3, and 0.1 mM EDTA in 10% D_2O.

The KirBac1.1 (residues 1–321) protein, including an N-terminal His10-tag and an HRV-3C protease recognition site, was expressed in C41(DE3) *E. coli* cells (Lucigen) and purified as described previously [43,47]. The cells were grown in deuterated M9 medium, and 50 mg/L of [methyl-^{13}C,3,3-$^{2}H_2$]-α-ketobutyric acid (for Ileδ1) was added 1 h prior to the induction [71]. First, the protein was solubilized with 30 mM of *n*-decyl-β-D-maltoside (DM) (Dojindo) and purified with HIS-Select resin (Sigma-Aldrich). After cleavage of the His10-tag with HRV-3C protease (Novagen), the protein was further purified by size exclusion chromatography on a Superdex 200 Increase 10/300 GL (GE). The DM was exchanged on a DEAE sepharose column (GE) to *n*-dodecyl-d25-β-D-maltoside (FB Reagents). The NMR sample consisted of 0.2–0.4 mM KirBac1.1 (as a monomer), 10 mM HEPES-KOH (pD 8.0), 100 mM KCl, 1 mM EDTA, and 10 to 20 mM *n*-dodecyl-d25-β-D-maltoside in 99% D_2O. For the nanodisc reconstitution, a lipid mixture comprising 75% 1-palmitoyl-2-oleoyl-*sn*-glycero-3-phosphoethanolamine (POPE) and 25% 1-palmitoyl-2-oleoyl-*sn*-glycero-3-phospho-(1′-*rac*-glycerol) (POPG) (w/w) (Avanti Polar Lipid) was dissolved in 30 mM DM. The MSP1 protein was prepared as previously described [74,75]. The His-tagged KirBac1.1 protein, lipid, and MSP1 were mixed to the respective final concentrations of 50 μM (as a tetramer), 14 mM, and 280 μM, dissolved in about 30 mM DM, and incubated at 4 °C for 1.5 h. The KirBac1.1-rHDL nanodisc was assembled by removing the DM by adding 80% (w/v) of Bio-Beads SM-2 (Bio-Rad) and mixing at 4 °C for 1.5 h. The KirBac1.1-rHDL was further purified with HIS-Select resin (Sigma-Aldrich). After cleavage of the His10-tag with HRV-3C protease (Novagen), the protein was further purified by size exclusion chromatography on a Superdex 200 Increase 10/300 GL (GE). The NMR sample consisted of 22 μM KirBac1.1-nanodisc, 10 mM HEPES-KOH (pD 8.0), 100 mM KCl, and 1 mM EDTA in 99% D_2O.

All mutants were constructed with a QuikChange® Site-directed Mutagenesis Kit (Agilent Technologies).

4.2. NMR analyses

All experiments were performed on Bruker Avance 400, 600, 800, or 950 MHz spectrometers equipped with room temperature BBFO (400 MHz), room temperature triple resonance (600 MHz), or cryogenic triple resonance (600, 800, and 950 MHz) probes. All spectra were processed by the Bruker TopSpin 2.1 or 3.1 software, and the data were analyzed using Sparky (T. D. Goddard and D. G. Kneller, Sparky 3, University of California, San Francisco, CA). The average noise level was calculated by dividing the peak-to-peak noise by 2.5, which was measured from a signal-free region. The ^{1}H chemical shifts were referenced to the methyl ^{1}H of 3-(trimethylsilyl)-1-propanesulfonic acid sodium salt, and the ^{13}C and ^{15}N chemical shifts were referenced indirectly [76]. The CW field strength was calibrated using the pulse sequence developed by Guenneugues *et al.* [77].

The ^{15}N-selective HSFPT ^{1}H 1D spectra for [^{15}N-indole] DL-Tryptophan were recorded at 25 °C with the Bruker Avance 400 spectrometer. The CW field strengths were varied between 11 and 218 Hz, and the values of the transfer time τ were varied between 2 and 33 ms. The ^{13}C-selective HSFPT ^{1}H 1D spectra for [ring-2-^{13}C] L-Histidine were recorded at 25 °C with the Bruker Avance 400 spectrometer. The CW field strengths were varied between 12 and 207 Hz, and the values of the transfer time τ were varied between 1 and 32 ms. The ^{13}C-selective HSFPT ^{1}H 1D spectra for [2-^{13}C] sodium acetate were recorded at 25 °C with the Bruker Avance 400 spectrometer. The CW field strengths were varied between 13 and 199 Hz, and the values of the transfer time τ were varied between 1 and 32 ms. For the measurement of the ^{13}C-frequency-swept HSFPT ^{1}H 1D spectra, the ^{13}C carrier frequencies were varied between −400 and + 400 Hz from the methyl ^{13}C resonance frequency in increments of 5 Hz. The CW field strength was set to 70 Hz, and the value of the transfer time τ was set to 11 ms.

The ^{15}N-selective HSFPT ^{1}H 1D spectra for [Val-^{15}N] MBP were recorded at 20 °C with the Bruker Avance 600 spectrometer. The CW field strength was set to 50 Hz, and the value of the transfer time τ was set to 12 ms. The reference ^{1}H-^{15}N HSQC spectrum was recorded with 1024 (^{1}H) and 256 (^{15}N) points (128 *cosine* and 128 *sine* components), and the acquisition times were set to 61.0 and 52.6 ms, respectively. The pulse sequence of the reference HSQC is implemented in the TopSpin2.1 software (Bruker) as 'hsqcfpf3gpphwg'. The ^{15}N-frequency-swept HSFPT ^{1}H 1D spectra were recorded at 20 °C with the Bruker Avance 600 and 950 spectrometers. The ^{15}N carrier frequencies were varied in increments of 10 Hz. The CW field strength was set to 50 Hz, and the value of the transfer time τ was set to 12 ms. The assignments of the Val amide signals were obtained from the previous report [78].

The ^{13}C-selective HSFPT ^{1}H 1D spectra for [u-^{2}H, Ileδ1-$^{13}CH_3$] MBP were recorded at 4 °C with the Bruker Avance 400 and 600 spectrometers. The CW field strength was set to 70 Hz, and the value of the transfer time τ was set to 11 ms, unless otherwise noted. The reference ^{1}H-^{13}C HMQC spectrum was recorded with 1024 (^{1}H) and 128 (^{13}C) points (64 *cosine* and 64 *sine* components), and the acquisition times were set to 61.0 and 60.6 ms, respectively. The ^{13}C-frequency-swept HSFPT ^{1}H 1D spectra were recorded at 20 °C with the Bruker Avance 600 and 950 spectrometers. The ^{13}C carrier frequencies were varied in increments of 5 Hz. The CW field strength was set to 70 Hz, and the value of the trans-

fer time τ was set to 11 ms. The assignments of the Ile methyl signals were obtained from the previous report [78].

The ^{13}C SQ CPMG RD experiments for the T4 lysozyme mutant were recorded at 4 °C with the Bruker Avance 600 spectrometer [33]. The constant-time CPMG relaxation period T was set to 40 ms, and the ν_{CPMG} values were varied between 50 and 1000 Hz. The ^{15}N SQ and ^{1}H SQ CPMG RD experiments for the FF domain were recorded at 25 °C with the Bruker Avance 600 spectrometer [36,37]. The constant-time CPMG relaxation period T was set to 40 ms, and the ν_{CPMG} values were varied between 50 and 1000 Hz. The values of the effective relaxation rates measured in the presence of a ν_{CPMG} Hz CPMG pulse train, $R_{2,eff}(\nu_{CPMG})$, were calculated using the following equation, where $I(\nu_{CPMG})$ and $I(0)$ represent the peak intensities with and without the relaxation period T, respectively.

$$R_{2,\mathrm{eff}}(\nu_{\mathrm{CPMG}}) = -\frac{1}{T} ln\left\{\frac{I(\nu_{\mathrm{CPMG}})}{I(0)}\right\} \tag{8}$$

We calculated the theoretical values for $R_{2,eff}$ using the Carver-Richard formula [79], where k_{ex} represents the exchange rate, $\Delta\omega$ represents the SQ chemical shift difference, and p_{min} represents the population of the minor state.

$$\begin{aligned} R_{2,\mathrm{eff}} &= R_{2,0} + \tfrac{k_{\mathrm{ex}}}{2} - \nu_{\mathrm{CPMG}}\cosh^{-1}\left[D_+\cosh(\eta_+) - D_-\cos(\eta_-)\right] \\ \eta_\pm &= \tfrac{1}{2\sqrt{2}\nu_{\mathrm{CPMG}}}\left[\pm\Psi + \left(\Psi^2+\xi^2\right)^{1/2}\right]^{1/2} \\ D_\pm &= \tfrac{1}{2}\left[\pm 1 + \tfrac{\Psi+2\Delta\omega^2}{\left(\Psi^2+\xi^2\right)^{1/2}}\right] \\ \Psi &= {k_{\mathrm{ex}}}^2 - \Delta\omega^2 \\ \xi &= -2\Delta\omega k_{\mathrm{ex}}(1-2p_{\mathrm{min}}) \end{aligned} \tag{9}$$

The exchange parameters were extracted by minimizing the χ^2 function, where σ represents the error in the experimental measurement estimated from the average noise levels. In the global fitting procedure, we simultaneously analyzed the data from Val71γ2, Val103γ2, Val149γ2, and Ile150δ1 for the T4 lysozyme mutant; and Lys41, Tyr49, Ser50, Lys59, and Val67 for the FF domain. The optimization procedure was performed with the in-house-developed program written in the programming language, Python 2.7, supplemented with the extension modules, Numpy 1.7 and Scipy 0.11.0. Uncertainties of the parameters were estimated using a bootstrap procedure [80], where a set of 200 data sets was generated from randomly selected values, while keeping the total size of the data points the same.

$$\chi^2 = \sum \frac{\left(R_{2,\mathrm{eff}}^{\mathrm{exp}} - R_{2,\mathrm{eff}}^{\mathrm{calc}}\right)^2}{\left(\sigma_{R_{2,\mathrm{eff}}}\right)^2} \tag{10}$$

The ^{15}N CEST experiments for the FF domain A39G mutant were recorded at 5 °C with the Bruker Avance 600 spectrometer [13]. The relaxation period T_{relax} was set to 500 ms. The ^{15}N carrier frequencies were varied between 105.62 and 128.64 ppm in increments of 0.42 ppm (25 Hz), and the ^{15}N CW field of 26 Hz was applied during the period. The ^{13}C CEST experiments for the T4 lysozyme mutant were recorded at 4 °C with the Bruker Avance 600 spectrometer [39]. The relaxation period T_{relax} was set to 500 ms. The ^{13}C carrier frequencies were varied between 17.00 and 26.84 ppm in increments of 0.10 ppm (15 Hz), and the ^{13}C CW field of 15 Hz was applied during the period.

The ^{13}C-selective HSFPT ^{1}H-^{13}C MQ CPMG RD spectra for [u-^{2}H, Ileδ1-^{13}CH$_3$] KirBac1.1 were recorded at 20 °C with the Bruker Avance 600 and 800 spectrometers. The CW field strength was set to 90 Hz, and the value of the transfer time τ was set to 8 ms. The constant-time CPMG relaxation period T value was set to 20 ms for KirBac1.1 in the DDM micelles, and 10 ms for the KirBac1.1-nanodiscs. The ν_{CPMG} values were varied between 50 and 1000 Hz for KirBac1.1 in the DDM micelles, and between 100 and 1000 Hz for the KirBac1.1-nanodiscs. We calculated the theoretical values for $R_{MQ,eff}$ using the equation as previously described [38,81]. The exchange parameters were extracted by minimizing the χ^2 function (equation (10)). The optimization procedure was performed with the in-house-developed program written in the programming language, Python 2.7, supplemented with the extension modules, Numpy 1.7 and Scipy 0.11.0. Uncertainties of the parameters were estimated using a bootstrap procedure [80], where a group of 200 data sets was generated from randomly selected values, while keeping the total size of the data points the same. The ^{1}H-^{13}C HSQC and HMQC spectra for the peak shift analysis were recorded at 25 °C with the Bruker Avance 800 spectrometer.

4.3. Density matrix calculations

To describe the time-evolution of magnetization, we conducted density matrix calculations using the Liouville-von Neumann equation [9]. We considered a spin system in which the ^{1}H spin is weakly-coupled to the heteronucleus A (= ^{15}N or ^{13}C), through scalar coupling with the coupling constant, J. In the following calculations, the relaxation contributions were not incorporated. The Hamiltonian in the doubly rotating frame can be expressed by the following equation, where Ω_H and Ω_A denote the chemical shift offset frequencies for ^{1}H and A; and ω_{Hx}, ω_{Ax}, ω_{Hy}, and ω_{Ay} are the radio frequency field strengths along the $\times$ and y axes for ^{1}H and A.

$$\mathcal{H} = \Omega_H H_z + \Omega_A A_z + 2\pi J H_z A_z + \omega_{Hx}H_x + \omega_{Hy}H_y + \omega_{Ax}A_x + \omega_{Ay}A_y \tag{11}$$

The basis sets used for describing the ^{1}H-A (A = ^{15}N or ^{13}C) two-spin system can be expressed by the following equation. Using these basis sets, the Cartesian product operators were described by the direct products of these basis sets [9].

$$\begin{aligned} A_x &= \tfrac{1}{2}\begin{bmatrix} 0 & 1 \\ 1 & 0 \end{bmatrix} \quad H_x = \tfrac{1}{2}\begin{bmatrix} 0 & 1 \\ 1 & 0 \end{bmatrix} \\ A_y &= \tfrac{1}{2}\begin{bmatrix} 0 & -i \\ i & 0 \end{bmatrix} \quad H_y = \tfrac{1}{2}\begin{bmatrix} 0 & -i \\ i & 0 \end{bmatrix} \\ A_z &= \tfrac{1}{2}\begin{bmatrix} 1 & 0 \\ 0 & -1 \end{bmatrix} \quad H_z = \tfrac{1}{2}\begin{bmatrix} 1 & 0 \\ 0 & -1 \end{bmatrix} \end{aligned} \tag{12}$$

To describe the methyl ^{1}H$_3$-^{13}C spin system, we used the bases of the eigenfunctions for the methyl ^{1}H$_3$-^{13}C spin system introduced by Kay and co-workers [26]. The Cartesian product operators were described by the direct products of these basis sets. For separately analyzing the fast and slow relaxing components of the in-phase H_y coherences, we defined and used the following operator bases; $H_y^{fast} = \frac{\sqrt{3}}{2} i(-|1\rangle\langle 2| + |2\rangle\langle 1| - |3\rangle\langle 4| + |4\rangle\langle 3|)$ and $H_y^{slow} = \frac{i}{2}(-2|2\rangle\langle 3| + 2|3\rangle\langle 2| - |5\rangle\langle 6| + |6\rangle\langle 5| + |7\rangle\langle 8| - |8\rangle\langle 7|)$.

$$C_x = \frac{1}{2}\begin{bmatrix} 0 & 1 \\ 1 & 0 \end{bmatrix}$$

$$C_y = \frac{1}{2}\begin{bmatrix} 0 & -i \\ i & 0 \end{bmatrix}$$

$$C_z = \frac{1}{2}\begin{bmatrix} 1 & 0 \\ 0 & -1 \end{bmatrix}$$

$$H_x = \frac{1}{2}\begin{bmatrix} 0 & \sqrt{3} & 0 & 0 & 0 & 0 & 0 & 0 \\ \sqrt{3} & 0 & 2 & 0 & 0 & 0 & 0 & 0 \\ 0 & 2 & 0 & \sqrt{3} & 0 & 0 & 0 & 0 \\ 0 & 0 & \sqrt{3} & 0 & 0 & 0 & 0 & 0 \\ 0 & 0 & 0 & 0 & 0 & 1 & 0 & 0 \\ 0 & 0 & 0 & 0 & 1 & 0 & 0 & 0 \\ 0 & 0 & 0 & 0 & 0 & 0 & 0 & -1 \\ 0 & 0 & 0 & 0 & 0 & 0 & -1 & 0 \end{bmatrix}$$

$$H_y = \frac{1}{2}\begin{bmatrix} 0 & -\sqrt{3}i & 0 & 0 & 0 & 0 & 0 & 0 \\ \sqrt{3}i & 0 & -2i & 0 & 0 & 0 & 0 & 0 \\ 0 & 2i & 0 & -\sqrt{3}i & 0 & 0 & 0 & 0 \\ 0 & 0 & \sqrt{3}i & 0 & 0 & 0 & 0 & 0 \\ 0 & 0 & 0 & 0 & 0 & -i & 0 & 0 \\ 0 & 0 & 0 & 0 & i & 0 & 0 & 0 \\ 0 & 0 & 0 & 0 & 0 & 0 & 0 & i \\ 0 & 0 & 0 & 0 & 0 & 0 & -i & 0 \end{bmatrix} \quad (13)$$

$$H_z = \frac{1}{2}\begin{bmatrix} 3 & 0 & 0 & 0 & 0 & 0 & 0 & 0 \\ 0 & 1 & 0 & 0 & 0 & 0 & 0 & 0 \\ 0 & 0 & -1 & 0 & 0 & 0 & 0 & 0 \\ 0 & 0 & 0 & -3 & 0 & 0 & 0 & 0 \\ 0 & 0 & 0 & 0 & 1 & 0 & 0 & 0 \\ 0 & 0 & 0 & 0 & 0 & -1 & 0 & 0 \\ 0 & 0 & 0 & 0 & 0 & 0 & 1 & 0 \\ 0 & 0 & 0 & 0 & 0 & 0 & 0 & -1 \end{bmatrix}$$

The evolution of the density matrix at time t, $\sigma(t)$, can be described by the solution of the Liouville–von Neumann equation. The expectation value for an operator O is given by $\mathrm{Tr}\{\sigma O\}$.

$$\sigma(t+\tau) = \exp(-i\mathcal{H}\tau)\sigma(t)\exp(i\mathcal{H}\tau) \quad (14)$$

We set the initial condition to be equal to a transverse ^{1}H magnetization $-H_y$, which is created by the first $\pi/2$ H_x excitation pulse applied on a ^{1}H equilibrium magnetization. In the typical calculations for describing the HSFPT scheme, the following conditions were used; $\omega_{Ax} = \omega_{rf}$, $\omega_{Hx} = \omega_{Hy} = \omega_{Ay} = 0$, and $\Omega_H = \Omega_A = 0$, where ω_{rf} represents the strength of the weak CW field.

To evaluate the HSFPT efficiency in the presence of relaxation, we calculated a homogenous master equation for the ^{1}H-^{15}N two-spin system following the formalism introduced by Allard *et al.* [29]. The overall rotational correlation time was set to 0, 10, 30, or 50 ns, and the magnetic field strength was set to 14.1 Tesla (600 MHz ^{1}H frequency). The other parameters for calculating the relaxation matrix elements were set to the same values as described in the original paper. The CW field strengths were varied between 0 and 150 Hz, and the values of the transfer time τ were varied between 0 and 30 ms.

4.4. $^{86}Rb^+$ intake assay of KirBac1.1

$^{86}Rb^+$ intake assays were performed as previously described [44,47]. All experiments were performed on liposomes composed POPE and POPG (POPE:POPG = 3:1, Avanti Polar Lipids). The purified KirBac1.1 protein was reconstituted into liposomes at a protein-to-lipid ratio of 1:1000 (w/w). The amounts of $^{86}Rb^+$ intake were normalized to the maximal $^{86}Rb^+$ intake, measured after the addition of 1.0 μg/mL valinomycin (Calbiochem).

4.5. Molecular dynamics simulations

The all-atom model of KirBac1.1 in the closed conformation was constructed with the CHARMM-GUI Membrane Builder [82,83], based on the crystal structure of KirBac1.1 (PDB ID: 1P7B) [43]. To construct the all-atom model of KirBac1.1 in the open conformation, we first constructed the homology model using the crystal structure of the KirBac3.1 S129R mutant (PDB ID: 3ZRS) by SWISS-MODEL [49,84], and then constructed the all-atom model with the CHARMM-GUI Membrane Builder [82,83], based on the homology model. The structures were embedded into a 75% POPE and 25% POPG bilayer, and solvated in a periodic water box with a size of $101 \times 101 \times 126$ Å^3 using TIP3P water molecules. The system was neutralized with about 150 mM KCl. Molecular dynamics simulations were performed using the NAMD2.12 software [85] and the CHARMM36m parameter set [86]. A cutoff distance of 12 Å was used for the van der Waals and short-range electrostatic interactions, and the long-range electrostatic interactions were computed with the particle-mesh Ewald method [87]. Bonds containing hydrogen atoms were restrained with the SHAKE algorithm [88]. Bonded and electrostatic interactions were computed every 2 fs. The equilibration of the system was performed according to the standard setting of the CHARMM-GUI Membrane Builder at 310 K, and the production simulations were performed for 20 ns, at 1 atm and 310 K. The trajectories were analyzed with the VMD 1.9.3 software [89].

Acknowledgements

This work was supported in part by the Japan Agency for Medical Research and Development (AMED) under Grant Number JP18ae0101046 (to I.S.) and the Ministry of Education, Culture, Sports, Science and Technology (MEXT)/Japan Society for the Promotion of Science KAKENHI, Grant Number JP17H06097 (to I.S.). The NMR experiments at 950 MHz were performed at Yokohama City University of NMR platform supported by MEXT, Japan. The $^{86}Rb^+$ intake assays of KirBac1.1 were performed with the support of the Radioisotope Center, The University of Tokyo.

Competing financial interests

The authors declare no competing financial interests.

Appendix A. Supplementary material

Supplementary data to this article can be found online at https://doi.org/10.1016/j.jmr.2019.05.004.

References

[1] J. Jeener, B.H. Meier, P. Bachmann, R.R. Ernst, Investigation of exchange processes by two-dimensional NMR spectroscopy, J. Chem. Phys. 71 (1979) 4546–4553.
[2] R.R. Ernst, G. Bodenhausen, Alexander Wokaun, Principles of Nuclear Magnetic Resonance in One and Two Dimensions, Clarendon Press, Oxford, 1987.
[3] D.C. Muchmore, L.P. McIntosh, C.B. Russell, D.E. Anderson, F.W. Dahlquist, Expression and nitrogen-15 labeling of proteins for proton and nitrogen-15 nuclear magnetic resonance, Methods Enzymol. 177 (1989) 44–73.
[4] G.M. Clore, A.M. Gronenborn, Multidimensional heteronuclear nuclear magnetic resonance of proteins, Methods Enzymol. 239 (1994) 349–363.
[5] K.H. Gardner, L.E. Kay, The use of ^{2}H, ^{13}C, ^{15}N multidimensional NMR to study the structure and dynamics of proteins, Annu. Rev. Biophys. Biomol. Struct. 27 (1998) 357–406.
[6] V. Tugarinov, P.M. Hwang, L.E. Kay, Nuclear magnetic resonance spectroscopy of high-molecular-weight proteins, Annu. Rev. Biochem. 73 (2004) 107–146.

[7] S.J. Opella, F.M. Marassi, Applications of NMR to membrane proteins, Arch. Biochem. Biophys. 628 (2017) 92–101.
[8] S. Reckel, F. Löhr, V. Dötsch, In-cell NMR spectroscopy, ChemBioChem 6 (2005) 1601–1606.
[9] J. Cavanagh, W.J. Fairbrother, A.G. Palmer III, M. Rance, N.J. Skelton, Protein NMR Spectroscopy: Principles and Practice, second ed., Academic Press, 2007.
[10] H.Y. Carr, E.M. Purcell, Effects of diffusion on free precession in nuclear magnetic resonance experiments, Phys. Rev. 94 (1954) 630–638.
[11] Z. Luz, S. Meiboom, Nuclear magnetic resonance study of the protolysis of trimethylammonium ion in aqueous solution—order of the reaction with respect to solvent, J. Chem. Phys. 39 (1963) 366–370.
[12] J.P. Loria, M. Rance, A.G. Palmer, A relaxation-compensated Carr - Purcell - Meiboom - Gill sequence for characterizing chemical exchange by NMR spectroscopy, J. Am. Chem. Soc. 121 (1999) 2331–2332.
[13] P. Vallurupalli, G. Bouvignies, L.E. Kay, Studying "invisible" excited protein states in slow exchange with a major state conformation, J. Am. Chem. Soc. 134 (2012) 8148–8161.
[14] S. Imai, M. Osawa, K. Takeuchi, I. Shimada, Structural basis underlying the dual gate properties of KcsA, Proc. Natl. Acad. Sci. U. S. A. 107 (2010) 6216–6221.
[15] Y. Kofuku, T. Ueda, J. Okude, Y. Shiraishi, K. Kondo, M. Maeda, H. Tsujishita, I. Shimada, Efficacy of the β_2-adrenergic receptor is determined by conformational equilibrium in the transmembrane region, Nat. Commun. 3 (2012) 1045.
[16] A. Mochizuki, A. Saso, Q. Zhao, S. Kubo, N. Nishida, I. Shimada, Balanced regulation of redox status of intracellular thioredoxin revealed by in-Cell NMR, J. Am. Chem. Soc. 140 (2018) 3784–3790.
[17] R. Huang, Z.A. Ripstein, J.L. Rubinstein, L.E. Kay, Cooperative subunit dynamics modulate p97 function, Proc. Natl. Acad. Sci.. U.S.A. 116 (2018).
[18] J. Stelten, D. Leibfritz, Highly selective 1D CH correlations, Magn. Reson. Chem. 33 (1995) 827–830.
[19] E. Chiarparin, P. Pelupessy, G. Bodenhausen, Selective cross-polarization in solution state NMR, Mol. Phys. 95 (1998) 759–767.
[20] P. Pelupessy, E. Chiarparin, Hartmann-Hahn polarization transfer in liquids: an ideal tool for selective experiments, Concepts Magn. Reson. 12 (2000) 103–124.
[21] F. Ferrage, T.R. Eykyn, G. Bodenhausen, Frequency-switched single-transition cross-polarization: a tool for selective experiments in biomolecular NMR, ChemPhysChem 5 (2004) 76–84.
[22] D.M. Korzhnev, V.Y. Orekhov, L.E. Kay, Off-resonance $R_{1\rho}$ NMR studies of exchange dynamics in proteins with low spin-lock fields: an application to a Fyn SH3 domain, J. Am. Chem. Soc. 127 (2005) 713–721.
[23] A.L. Hansen, E.N. Nikolova, A. Casiano-Negroni, H.M. Al-Hashimi, Extending the range of microsecond-to-millisecond chemical exchange detected in labeled and unlabeled nucleic acids by selective carbon $R_{1\rho}$ NMR spectroscopy, J. Am. Chem. Soc. 131 (2009) 3818–3819.
[24] E. Walinda, D. Morimoto, M. Shirakawa, K. Sugase, F_1F_2-selective NMR spectroscopy, J. Biomol. NMR. 68 (2017) 41–52.
[25] V. Tugarinov, P.M. Hwang, J.E. Ollerenshaw, L.E. Kay, Cross-correlated relaxation enhanced ^{1}H–^{13}C NMR spectroscopy of methyl groups in very high molecular weight proteins and protein complexes, J. Am. Chem. Soc. 125 (2003) 10420–10428.
[26] J.E. Ollerenshaw, V. Tugarinov, L.E. Kay, Methyl TROSY: explanation and experimental verification, Magn. Reson. Chem. 41 (2003) 843–852.
[27] E.R. Rey Castellanos, D.P. Frueh, J. Wist, Selective polarization transfer using a single rf field, J. Chem. Phys. 129 (2008).
[28] G.A. Morris, R. Freeman, Enhancement of nuclear magnetic resonance signals by polarization transfer, J. Am. Chem. Soc. 101 (1979) 760–762.
[29] P. Allard, M. Helgstrand, T. Härd, The complete homogeneous master equation for a heteronuclear two-spin system in the basis of cartesian product operators, J. Magn. Reson. 134 (1998) 7–16.
[30] D.F. Hansen, P. Neudecker, P. Vallurupalli, F.A.A. Mulder, L.E. Kay, Determination of Leu side-chain conformations in excited protein states by NMR relaxation dispersion, J. Am. Chem. Soc. 132 (2010) 42–43.
[31] D.F. Hansen, P. Neudecker, L.E. Kay, Determination of isoleucine side-chain conformations in ground and excited states of proteins from chemical shifts, J. Am. Chem. Soc. 132 (2010) 7589–7591.
[32] D.F. Hansen, L.E. Kay, Determining valine side-chain rotamer conformations in proteins from methyl ^{13}C chemical shifts: application to the 360 kDa half-proteasome, J. Am. Chem. Soc. 133 (2011) 8272–8281.
[33] P. Lundström, P. Vallurupalli, T.L. Religa, F.W. Dahlquist, L.E. Kay, A single-quantum methyl ^{13}C-relaxation dispersion experiment with improved sensitivity, J. Biomol. NMR. 38 (2007) 79–88.
[34] G. Bouvignies, P. Vallurupalli, D.F. Hansen, B.E. Correia, O. Lange, A. Bah, R.M. Vernon, F.W. Dahlquist, D. Baker, L.E. Kay, Solution structure of a minor and transiently formed state of a T4 lysozyme mutant, Nature 477 (2011) 111–114.
[35] Y. Toyama, H. Kano, Y. Mase, M. Yokogawa, M. Osawa, I. Shimada, Dynamic regulation of GDP binding to G proteins revealed by magnetic field-dependent NMR relaxation analyses, Nat. Commun. 8 (2017) 14523.
[36] M. Tollinger, N.R. Skrynnikov, F.A.A. Mulder, J.D. Forman-Kay, L.E. Kay, Slow dynamics in folded and unfolded states of an SH3 domain, J. Am. Chem. Soc. 123 (2001) 11341–11352.
[37] R. Ishima, D.A. Torchia, Extending the range of amide proton relaxation dispersion experiments in proteins using a constant-time relaxation-compensated CPMG approach, J. Biomol. NMR. 25 (2003) 243–248.
[38] D.M. Korzhnev, K. Kloiber, V. Kanelis, V. Tugarinov, L.E. Kay, Probing slow dynamics in high molecular weight proteins by methyl-TROSY NMR spectroscopy: application to a 723-residue enzyme, J. Am. Chem. Soc. 126 (2004) 3964–3973.
[39] G. Bouvignies, L.E. Kay, A 2D ^{13}C-CEST experiment for studying slowly exchanging protein systems using methyl probes: an application to protein folding, J. Biomol. NMR. 53 (2012) 303–310.
[40] D.M. Korzhnev, T.L. Religa, P. Lundström, A.R. Fersht, L.E. Kay, The folding pathway of an FF domain: characterization of an on-pathway intermediate state under folding conditions by ^{15}N, $^{13}C^{\alpha}$ and ^{13}C-methyl relaxation dispersion and ^{1}H/^{2}H-exchange NMR S, J. Mol. Biol. 372 (2007) 497–512.
[41] D.M. Korzhnev, T.L. Religa, W. Banachewicz, A.R. Fersht, L.E. Kay, A transient and low-populated protein-folding intermediate at atomic resolution, Science 329 (2010) 1312–1316.
[42] S.R. Durell, H.R. Guy, A family of putative Kir potassium channels in prokaryotes, BMC Evol. Biol. 1 (2001) 14.
[43] A. Kuo, J.M. Gulbis, J.F. Antcliff, T. Rahman, E.D. Lowe, J. Zimmer, J. Cuthbertson, F.M. Ashcroft, T. Ezaki, D.A. Doyle, Crystal structure of the potassium channel KirBac1.1 in the closed state, Science 300 (2003) 1922–1926.
[44] D. Enkvetchakul, J. Bhattacharyya, I. Jeliazkova, D.K. Groesbeck, C.A. Cukras, C. G. Nichols, Functional characterization of a prokaryotic Kir channel, J. Biol. Chem. 279 (2004) 47076–47080.
[45] W.W.L. Cheng, D. Enkvetchakul, C.G. Nichols, KirBac1. 1: It's an inward rectifying potassium channel, J. Gen. Physiol. 133 (2009) 295–305.
[46] S. Wang, R. Vafabakhsh, W.F. Borschel, T. Ha, C.G. Nichols, Structural dynamics of potassium-channel gating revealed by single-molecule FRET, Nat. Struct. Mol. Biol. 23 (2016) 31–36.
[47] Y. Toyama, M. Osawa, M. Yokogawa, I. Shimada, NMR method for characterizing microsecond-to-millisecond chemical exchanges utilizing differential multiple-quantum relaxation in high molecular weight proteins, J. Am. Chem. Soc. 138 (2016) 2302–2311.
[48] N.R. Skrynnikov, F.W. Dahlquist, L.E. Kay, Reconstructing NMR spectra of "invisible" excited protein states using HSQC and HMQC experiments, J. Am. Chem. Soc. 124 (2002) 12352–12360.
[49] V.N. Bavro, R. De Zorzi, M.R. Schmidt, J.R.C. Muniz, L. Zubcevic, M.S.P. Sansom, C. Vénien-Bryan, S.J. Tucker, Structure of a KirBac potassium channel with an open bundle crossing indicates a mechanism of channel gating, Nat. Struct. Mol. Biol. 19 (2012) 158–164.
[50] T.H. Bayburt, Y.V. Grinkova, S.G. Sligar, Self-assembly of discoidal phospholipid bilayer nanoparticles with membrane scaffold proteins, Nano Lett. 2 (2002) 853–856.
[51] T.K. Ritchie, Y.V. Grinkova, T.H. Bayburt, I.G. Denisov, J.K. Zolnerciks, W.M. Atkins, S.G. Sligar, Reconstitution of membrane proteins in phospholipid bilayer nanodiscs, in: Methods Enzymol, first ed., Elsevier Inc., 2009, pp. 211–231.
[52] Y. Qi, J. Lee, J.B. Klauda, W. Im, CHARMM-GUI *Nanodisc Builder* for modeling and simulation of various nanodisc systems, J. Comput. Chem. 40 (2019) 893–899.
[53] M.J. Smith, C.B. Marshall, F.X. Theillet, A. Binolfi, P. Selenko, M. Ikura, Real-time NMR monitoring of biological activities in complex physiological environments, Curr. Opin. Struct. Biol. 32 (2015) 39–47.
[54] W. Kwiatkowski, R. Riek, Chemical shift-dependent apparent scalar couplings: An alternative concept of chemical shift monitoring in multi-dimensional NMR experiments, J. Biomol. NMR. 25 (2003) 281–290.
[55] C. Ritter, T. Lührs, W. Kwiatkowski, R. Riek, 3d Trosy-Hnca coded cb and Trosy-Hnca coded co experiments: triple resonance nmr experiments with two sequential connectivity pathways and high sensitivity, J. Biomol. NMR. 28 (2004) 289–294.
[56] R. Keller, C.R.R. Grace, R. Riek, Fast multidimensional NMR spectroscopy by spin-state selective off-resonance decoupling (SITAR), Magn. Reson. Chem. 44 (2006) 196–205.
[57] K. Pervushin, R. Riek, G. Wider, K. Wuthrich, Attenuated T_2 relaxation by mutual cancellation of dipole-dipole coupling and chemical shift anisotropy indicates an avenue to NMR structures of very large biological macromolecules in solution, Proc. Natl. Acad. Sci. 94 (1997) 12366–12371.
[58] R. Riek, G. Wider, K. Pervushin, K. Wüthrich, Polarization transfer by cross-correlated relaxation in solution NMR with very large molecules, Proc. Natl. Acad. Sci. U. S. A. 96 (1999) 4918–4923.
[59] R. Riek, J. Fiaux, E.B. Bertelsen, A.L. Horwich, K. Wüthrich, Solution NMR techniques for large molecular and supramolecular structures, J. Am. Chem. Soc. 124 (2002) 12144–12153.
[60] K. Bromek, D. Lee, R. Hauhart, M. Krych-Goldberg, J.P. Atkinson, P.N. Barlow, K. Pervushin, Polychromatic selective population inversion for TROSY experiments with large proteins, J. Am. Chem. Soc. 127 (2005) 405–411.
[61] N. Khaneja, T. Reiss, B. Luy, S.J. Glaser, Optimal control of spin dynamics in the presence of relaxation, J. Magn. Reson. 162 (2003) 311–319.
[62] N. Khaneja, B. Luy, S.J. Glaser, Boundary of quantum evolution under decoherence, Proc. Natl. Acad. Sci. 100 (2003) 13162–13166.
[63] N. Khaneja, J.-S. Li, C. Kehlet, B. Luy, S.J. Glaser, Broadband relaxation-optimized polarization transfer in magnetic resonance, Proc. Natl. Acad. Sci. 101 (2004) 14742–14747.
[64] Y. Liu, J.H. Prestegard, Multi-dimensional NMR without coherence transfer: minimizing losses in large systems, J. Magn. Reson. 212 (2011) 289–298.
[65] B.F. Volkman, D. Lipson, D.E. Wemmer, D. Kern, Two-state allosteric behavior in a single-domain signaling protein, Science 291 (2001) 2429–2433.
[66] F. Massi, C. Wang, A.G. Palmer, Solution NMR and computer simulation studies of active site loop motion in triosephosphate isomerase, Biochemistry 45 (2006) 10787–10794.

[67] D.F. Hansen, D. Yang, H. Feng, Z. Zhou, S. Wiesner, Y. Bai, L.E. Kay, An exchange-free measure of ^{15}N transverse relaxation: an NMR spectroscopy application to the study of a folding intermediate with pervasive chemical exchange, J. Am. Chem. Soc. 129 (2007) 11468–11479.
[68] A.G. Palmer, C.D. Kroenke, J.P. Loria, NMR methods for quantifying microsecond-to-millisecond motions in biological macromolecules, Methods Enzym. 339 (2001) 204–238.
[69] M.T. Lin, L.J. Sperling, H.L. Frericks Schmidt, M. Tang, R.I. Samoilova, T. Kumasaka, T. Iwasaki, S.A. Dikanov, C.M. Rienstra, R.B. Gennis, A rapid and robust method for selective isotope labeling of proteins, Methods 55 (2011) 370–378.
[70] M.T. Lin, R. Fukazawa, Y. Miyajima-Nakano, S. Matsushita, S.K. Choi, T. Iwasaki, R.B. Gennis, *Escherichia coli* auxotroph host strains for amino acid-selective isotope labeling of recombinant proteins, in: Methods Enzymol, first ed., Elsevier Inc., 2015, pp. 45–66.
[71] N.K. Goto, K.H. Gardner, G.A. Mueller, R.C. Willis, L.E. Kay, A robust and cost-effective method for the production of Val, Leu, Ile (δ1) methyl-protonated ^{15}N-, ^{13}C-, ^{2}H-labeled proteins, J. Biomol. NMR. 13 (1999) 369–374.
[72] P. Gans, O. Hamelin, R. Sounier, I. Ayala, M.A. Durá, C.D. Amero, M. Noirclerc-Savoye, B. Franzetti, M.J. Plevin, J. Boisbouvier, Stereospecific isotopic labeling of methyl groups for NMR spectroscopic studies of high-molecular-weight proteins, Angew. Chemie Int. Ed. 49 (2010) 1958–1962.
[73] P. Vallurupalli, D.F. Hansen, P. Lundström, L.E. Kay, CPMG relaxation dispersion NMR experiments measuring glycine ^{1}H$^{\alpha}$ and ^{13}C$^{\alpha}$ chemical shifts in the "invisible" excited states of proteins, J. Biomol. NMR. 45 (2009) 45–55.
[74] C. Yoshiura, Y. Kofuku, T. Ueda, Y. Mase, M. Yokogawa, M. Osawa, Y. Terashima, K. Matsushima, I. Shimada, NMR analyses of the interaction between CCR5 and its ligand using functional reconstitution of CCR5 in lipid bilayers, J. Am. Chem. Soc. 132 (2010) 6768–6777.
[75] S. Imai, M. Osawa, K. Mita, S. Toyonaga, A. Machiyama, T. Ueda, K. Takeuchi, S. Oiki, I. Shimada, Functional equilibrium of the KcsA structure revealed by NMR, J. Biol. Chem. 287 (2012) 39634–39641.
[76] D. Wishart, C. Bigam, J. Yao, F. Abildgaard, H.J. Dyson, E. Oldfield, J. Markley, B. Sykes, ^{1}H, ^{13}C and ^{15}N chemical shift referencing in biomolecular NMR, J. Biomol. NMR. 6 (1995) 135–140.
[77] M. Guenneugues, P. Berthault, H. Desvaux, A method for determining B_1 field inhomogeneity. Are the biases assumed in heteronuclear relaxation experiments usually underestimated?, J Magn. Reson. 136 (1999) 118–126.
[78] K.H. Gardner, X. Zhang, K. Gehring, L.E. Kay, Solution NMR studies of a 42 KDa escherichia C oli maltose binding protein/β-cyclodextrin complex: chemical shift assignments and analysis, J. Am. Chem. Soc. 120 (1998) 11738–11748.
[79] J.P. Carver, R.E. Richards, A general two-site solution for the chemical exchange produced dependence of T_2 upon the carr-Purcell pulse separation, J. Magn. Reson. 6 (1972) 89–105.
[80] B. Efron, R. Tibshirani, Bootstrap methods for standard errors, confidence intervals, and other measures of statistical accuracy, Stat. Sci. 1 (1986) 54–75.
[81] D.M. Korzhnev, K. Kloiber, L.E. Kay, Multiple-quantum relaxation dispersion NMR spectroscopy probing millisecond time-scale dynamics in proteins: theory and application, J. Am. Chem. Soc. 126 (2004) 7320–7329.
[82] S. Jo, T. Kim, V.G. Iyer, W. Im, CHARMM-GUI: a web-based graphical user interface for CHARMM, J. Comput. Chem. 29 (2008) 1859–1865.
[83] J. Lee, X. Cheng, J.M. Swails, M.S. Yeom, P.K. Eastman, J.A. Lemkul, S. Wei, J. Buckner, J.C. Jeong, Y. Qi, S. Jo, V.S. Pande, D.A. Case, C.L. Brooks, A.D. MacKerell, J.B. Klauda, W. Im, CHARMM-GUI input generator for NAMD, GROMACS, AMBER, OpenMM, and CHARMM/OpenMM simulations using the CHARMM36 additive force field, J. Chem. Theory Comput. 12 (2016) 405–413.
[84] A. Waterhouse, M. Bertoni, S. Bienert, G. Studer, G. Tauriello, R. Gumienny, F.T. Heer, T.A.P. de Beer, C. Rempfer, L. Bordoli, R. Lepore, T. Schwede, SWISS-MODEL: homology modelling of protein structures and complexes, Nucleic Acids Res. 46 (2018) W296–W303.
[85] J.C. Phillips, R. Braun, W. Wang, J. Gumbart, E. Tajkhorshid, E. Villa, C. Chipot, R. D. Skeel, L. Kalé, K. Schulten, Scalable molecular dynamics with NAMD, J. Comput. Chem. 26 (2005) 1781–1802.
[86] J. Huang, S. Rauscher, G. Nawrocki, T. Ran, M. Feig, B.L. de Groot, H. Grubmüller, A.D. MacKerell, CHARMM36m: an improved force field for folded and intrinsically disordered proteins, Nat. Methods 14 (2017) 71–73.
[87] U. Essmann, L. Perera, M.L. Berkowitz, T. Darden, H. Lee, L.G. Pedersen, A smooth particle mesh Ewald method, J. Chem. Phys. 103 (1995) 8577–8593.
[88] J.-P. Ryckaert, G. Ciccotti, H.J. Berendsen, Numerical integration of the cartesian equations of motion of a system with constraints: molecular dynamics of *n*-alkanes, J. Comput. Phys. 23 (1977) 327–341.
[89] W. Humphrey, A. Dalke, K. Schulten, VMD: visual molecular dynamics, J. Mol. Graph. 14 (1996) 33–38.
[90] A.J. Shaka, P.B. Barker, R. Freeman, Computer-optimized decoupling scheme for wideband applications and low-level operation, J. Magn. Reson. 64 (1985) 547–552.
[91] D. Marion, M. Ikura, R. Tschudin, A. Bax, Rapid recording of 2D NMR spectra without phase cycling. Application to the study of hydrogen exchange in proteins, J. Magn. Reson. 85 (1989) 393–399.
[92] A.J. Shaka, J. Keeler, T. Frenkiel, R. Freeman, An improved sequence for broadband decoupling: WALTZ-16, J. Magn. Reson. 52 (1983) 335–338.
[93] H. Sun, L.E. Kay, V. Tugarinov, An optimized relaxation-based coherence transfer NMR experiment for the measurement of side-chain order in methyl-protonated, highly deuterated proteins, J. Phys. Chem. B 115 (2011) 14878–14884.